Two-dimensional elastic Bloch waves in helical periodic structures

Changwei Zhou, Fabien Treyssede

Two-dimensional elastic Bloch waves in helical periodic structures

C.W. Zhou[a], F. Treyssède[a,*]

[a]*GERS-GeoEND, Univ Gustave Eiffel, IFSTTAR, F-44344 Bouguenais, France*

Abstract

The goal of this paper is to investigate the propagation of two-dimensional elastic Bloch waves in helical periodic structures, obeying two discrete screw symmetries about the same axis. First, a three-dimensional coordinate system is built from the two helical directions of periodicity of the problem and the radial coordinate originating from the symmetry axis. The existence of Bloch waves in bi-helical structures can be justified owing to the independence of the metric tensor of the coordinate system on both helical coordinates. Considering the elastodynamic equilibrium equations, Bloch theorem is expressed in appropriate bases to project the vector wavefields, namely the covariant/contravariant bases of the bi-helical coordinate system (or, alternatively, the cylindrical basis). From a geometrical point of view, the three-dimensional unit cell is delimited by non-plane boundaries, which must be carefully parametrized. The so-called wave finite element method is then applied to numerically solve the Bloch wave eigenproblem and the implementation of the numerical method in a bi-helical system is detailed. Owing to the cylindrical nature of the geometry, the two-dimensional propagation constants are not independent to each other. The relationship between both constants is established. The calculation of wave mode properties (wavenumbers, group and energy velocities) is performed along the helical propagation directions, as well as the straight axial and circumferential directions. Numerical validations of the overall approach are carried out for cylindrical uniform tubes and a chiral nanotube. Finally, the method is applied to a complex multi-wire structure, often encountered in energy cables, consisting of two layers of helical wires twisted in opposite directions.

Keywords: wave; Bloch; periodic; helical; finite element; mode; screw symmetry

1. Introduction

The knowledge of elastic wave propagation characteristics is of great interest for the dynamic analysis of elongated structures, particularly in mid or high frequencies when the size of the structure is large compared to the wavelength. It provides the theoretical background necessary for many applications, such as nondestructive evaluation, structural health monitoring, vibration and noise reduction or statistical energy analysis for instance. Elongated structures can most often be considered as waveguides along one direction (beam-like structures) or two directions (plate- or tube-like structures), obeying continuous symmetry in these directions (*uniform* waveguides) or discrete symmetry (*periodic* waveguides). Waves in these structures are multimodal and dispersive. Modeling tools are required to understand the mechanism of their propagation. Typically, dispersion curves of phase and group velocities as functions of frequency help to identify wave modes that propagate in a frequency range of interest. In the case of periodic waveguides, bandgaps usually occur. These bandgaps provide valuable information for the design of phononic crystals to mitigate vibrations. Conversely, in nondestructive evaluation, the propagation distance of waves has to be maximized and these bandgaps have to be avoided.

The analysis of arbitrarily shaped three-dimensional structures requires numerical methods. Some of the most popular and efficient numerical techniques are based on finite element (FE) methods. The consideration of symmetries allows significant simplifications and reduces computation cost. A first FE approach consists in discretizing only the cross-section of the waveguide while describing analytically the direction of wave propagation. This approach has

*Corresponding author

Email address: fabien.treyssede@ifsttar.fr (F. Treyssède)

been applied under various names in the literature: the extended Ritz technique, the thin layer method for stratified waveguides in geophysics, the strip-element method, the semi-analytical finite element (SAFE) method or the scaled boundary finite element method in ultrasonics (see *e.g.* Refs. [1, 2, 3, 4, 5, 6, 7, 8]). This method allows studying cross-sections of arbitrary shapes. Since the eigenproblem is reduced on the cross-section (two-dimensional), the number of degrees of freedom is drastically reduced compared to a fully three-dimensional approach. However, this method is only applicable to uniform waveguides. When the structure is periodic, a second FE approach must be used. It consists in applying boundary conditions based on Bloch theorem in the finite element model of a single repetitive unit cell of the problem (see Refs. [9, 10, 11, 12, 13, 14, 15] for instance). This second approach is usually referred to as the Wave Finite Element Method (WFEM) in the literature and leads to an eigenproblem which is three-dimensional but reduced on a single unit cell. The WFEM can be used to study both uniform and periodic waveguides.

The above-cited references deal with waveguides having straight directions of symmetry (straight propagation directions), that is to say with translationally symmetric waveguides. A huge amount of works can be found in that case and an exhaustive review on this topic is beyond the scope of this paper. Conversely, the literature concerning the numerical modeling of curved waveguides is scarcer. One-directional uniform waveguides have been investigated with semi-analytical FE methods by accounting for continuous rotational symmetry, *i.e.* periodicity along a circumferential direction, occurring for instance in circular bars, toroidal pipes or tyres [16, 17, 18], as well as for continuous screw symmetry, *i.e.* periodicity along a helical direction, for the study of twisted bars, helical springs or multi-wire helical strands [19, 20, 21] (note that rotational symmetry can be viewed as a particular case of screw symmetry). One-directional curved waveguides have also been considered using the WFEM with discrete symmetry of rotational type [22] or screw type [23, 24, 25].

The case of two-directional periodic waveguides, curved in one or two directions, mainly concerns structures of cylindrical type. The WFEM has been used for modeling cylindrical panels involving discrete rotational symmetry along the circumferential direction, combined either with discrete translational symmetry [26, 27, 28] or screw symmetry [29]. Nanotubes involving two discrete screw symmetries have been investigated with the WFEM thanks to revisited periodic boundary conditions [30]. Considering multi-wire helical structures, the WFEM with discrete rotational symmetry has been combined with a semi-analytical finite element approach accounting for continuous screw symmetry [31].

This paper is concerned with two-dimensional elastic Bloch waves in helical structures obeying two discrete screw symmetries about the same axis. For simplicity, this type of periodicity will be termed as bi-helical in this paper. Since symmetries are of discrete type, SAFE-like methods are excluded and WFEM methods must be used. The type of problem considered here is similar to the nanotube investigation reported in Ref. [30], but the present paper adopts a different point of view. The analysis starts by building a coordinate system from the two helical directions of periodicity of the problem and the radial direction from the symmetry axis. The existence of Bloch waves in bi-helical structures can then be justified owing to the independence of the metric tensor of the curvilinear system on both helical coordinates. Because elastodynamics is governed by a vector wave equation, it is pointed out that Bloch theorem has to be expressed in appropriate bases to project the vector wavefields, namely the covariant/contravariant bases of the bi-helical system. It is shown that the more usual cylindrical basis can alternatively be used, which theoretically justifies the revisited boundary conditions proposed in Ref. [30]. The paper also details how to build the three-dimensional geometry of the bi-helical unit cell, which is delimited by non-plane boundaries and must hence be carefully parametrized.

The paper is organized as follows. Section 2 introduces a preliminary parametrization of the problem from a geometrical point of view. In Sec. 3, the so-called bi-helical coordinate system is built. The existence of two-dimensional Bloch waves is discussed in Sec. 4, as well as the appropriate bases for expressing the components of vector wavefields. Section 5 details the implementation of the WFEM and the calculation of modal properties (wavenumbers, group and energy velocities). Numerical results are presented in Secs. 6 and 7. Section 6 validates the overall approach with cylindrical tubes of uniform type as well as the chiral nanotube of Ref. [30]. Section 7 finally gives a more complex application to a multi-wire structure involving two layers of helical wires twisted in opposite directions.

As typical examples of bi-helical periodic structures, one could cite chiral nanotubes [32], grid-stiffened composite cylinders [33, 34, 35] or multi-wire cables [36, 37]. The main motivation of this paper is to investigate wave propagation in cable armors used in the energy industry. The armor of a cable provides the mechanical protection to the internal active part of the cable, including the conductors, and is typically multi-wired with one or two layers.

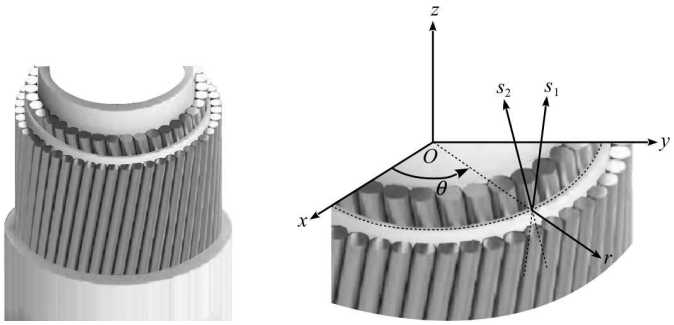

(a) (b)

Figure 1: Example of double armor cable. The internal active part is not represented. The armor consists of two protecting layers of helical steel wires twisted in opposite directions. The two layers are typically separated by an intermediate cylindrical sheath (also represented are the internal and external coatings surrounding the armor). (b) Sketch of the Cartesian coordinate system (x, y, z), the cylindrical system $(r, \theta, z,)$ and the bi-helical system (s_1, s_2, r). The curves s_1 and s_2 follow the outer and inner wires respectively. Here, the bi-helical system is plotted on the intermediate sheath.

In the latter case, the two protecting layers of wires are twisted in opposite directions, as shown in Fig. 1a, and the structure can be considered as a bi-helical periodic media. The analysis of wave propagation in cable armors is of potential interest for the development of nondestructive techniques to asses their structural integrity.

2. Preliminary parametrization and problem statement

Let us consider a periodic structure of cylindrical type having two directions of periodicity. The Cartesian coordinates are denoted as (x, y, z). The cylindrical coordinates are denoted as (r, θ, z), where r, θ and z are the radial, circumferential and axial directions respectively (with $x = r\cos\theta$ and $y = r\sin\theta$). We assume that both directions of periodicity are inclined with respect to θ and z and are hence helical, resulting in a bi-helical periodicity. These directions of periodicity are tangent to helical curves, denoted as s_1 and s_2. For clarity, the coordinate systems are sketched in Fig. 1b for the example of a double armor cable. As shown in Fig. 2, the unit cells of the periodic structure can therefore be delimited owing to two virtual layers of helices, each layer having their own helix parameters (in particular, the layers can be twisted in opposite directions).

Let us denote these two virtual layers as Layer **1** and Layer **2**, divided by N_1 helices oriented along s_1 and N_2 helices oriented along s_2 respectively. In the following, R_1 and ϕ_1 will denote the radius and the lay angle of the helices of Layer **1** ($\phi_1 \in [-\pi/2, \pi/2]$). Similarly, R_2 and ϕ_2 will denote the radius and the lay angle of the helices of Layer **2** ($\phi_2 \in [-\pi/2, \pi/2]$)). The helix lay angles are the angles measured with respect to the z-axis. In the remainder, subscripts α ($\alpha = 1, 2$) will be used to denote the layer index and the direction of periodicity.

The i-th helix of Layer α can be described by the position vector $\mathbf{R}_\alpha^{(i)}(s_\alpha)$ in the Cartesian orthonormal basis $(\mathbf{e}_x, \mathbf{e}_y, \mathbf{e}_z)$ as follows:

$$\mathbf{R}_\alpha^{(i)}(s_\alpha) = R_\alpha \cos\left(2\pi\frac{s_\alpha}{l_\alpha} + \theta_\alpha^{(i)}\right)\mathbf{e}_x + R_\alpha \sin\left(2\pi\frac{s_\alpha}{l_\alpha} + \theta_\alpha^{(i)}\right)\mathbf{e}_y + L_\alpha\frac{s_\alpha}{l_\alpha}\mathbf{e}_z \qquad (i = 1, \ldots, N_\alpha) \tag{1}$$

where $L_\alpha = 2\pi R_\alpha/\tan\phi_\alpha$ is equal to the helix step measured along the z-axis (straight) and $l_\alpha = 2\pi R_\alpha/\sin\phi_\alpha$ is the curvilinear step. The angle $\theta_\alpha^{(i)} = 2(i-1)\pi/N_\alpha$ is the phase angle of the i-th helix of Layer α. As illustrated in Fig. 2, the lay angle ϕ_α can be positive or negative. If $0 < \phi_\alpha < \pi/2$, the helices of Layer α are twisted around the z-axis in the counter-clockwise direction (right-handed), L_α and l_α are both positive. If $-\pi/2 < \psi_\alpha < 0$, the helices are twisted in the clockwise direction (left-handed), L_α and l_α are both negative. In any case, L_α and l_α always have the same sign, so that s_α always increases as z increases.

From Eq. (1), two particular cases can be noted:

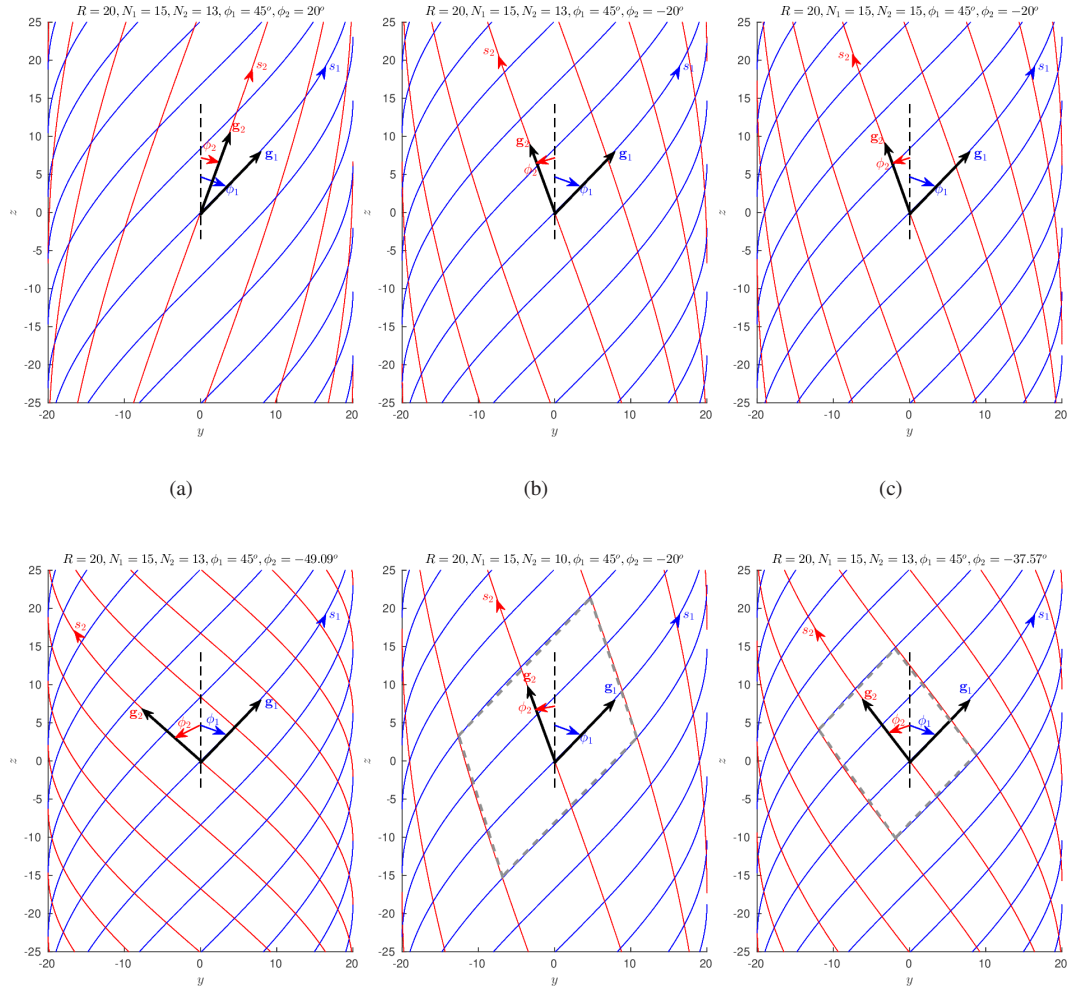

Figure 2: Example of bi-helical periodicity patterns. The unit cells are delimited by two virtual layers of helices, Layer **1** (blue) and Layer **2** (red). The helical coordinate curves are denoted as s_1 and s_2. The covariant basis vectors $\mathbf{g}_1$ and $\mathbf{g}_2$ are tangent to these curves (for clarity of figures, the modulus of $\mathbf{g}_1$ and $\mathbf{g}_2$ has been magnified). Various cases are represented: (a) pattern with no pure periodicity by rotation or translation ($\phi_1\phi_2 > 0$), (b) the same but with $\phi_1\phi_2 < 0$, (c) $N_1 = N_2$ (rotationally symmetric pattern), (d) $N_1L_2/N_2L_1 = -1$ (translationally symmetric pattern), (e) N_1/N_2 reducible to 3/2, (f) $N_1L_2/N_2L_1 = -3/2$. In examples (e)-(f), the symmetry is not achieved by a single unit cell but by a group of 3×2 unit cells (delimited by gray dashed lines in the figures).

- $\phi_\alpha = 0$ for a given direction (*i.e.* $1/l_\alpha = 0$ and $L_\alpha/l_\alpha = 1$): the direction α is straight ($s_\alpha = z$), corresponding to a symmetry of translational type,
- $\phi_\alpha = \pm\pi/2$ for a given direction (*i.e.* $l_\alpha = \pm 2\pi R_\alpha$ and $L_\alpha = 0$): the direction α is circumferential ($s_\alpha/R_\alpha = \pm\theta$), yielding a symmetry of rotational type.

Figure 2 shows examples of bi-helical periodicity patterns for different geometrical parameters. As shown later in Sec. 3.5, a rotational symmetry will always occur if the ratio N_1/N_2 is reducible, a translational symmetry will always occur if the ratio N_1L_2/N_2L_1 is rational. Figures 2a-b show two examples excluding these particular cases, which hence do not obey any periodicity of rotational or translational type. Figure 2c shows an example for $N_1 = N_2$, yielding a rotationally symmetric unit cell. Figure 2d shows an example such that $L_1/L_2 = \pm N_1/N_2$, yielding a translationally symmetric unit cell. In any case, the rotational or translational symmetry can be combined with a screw one provided that the other direction remains helical. As typical examples, one can cite armchair nanotubes and zigzag nanotubes [38], combining screw with translational and rotational symmetries respectively. Periodic structures in the latter case can be treated by the WFEM proposed in Ref [29] for pipes with helical patterns.

As discussed later in Sec. 3.5, translational or rotational symmetry can also be found by grouping more than one unit cell (the so-obtained period is not the minimum one) – see examples given by Figs. 2e-f. In Fig. 2e, the geometrical parameters have been chosen such that a group of 2×3 unit cells are rotationnaly symmetric. In Fig. 2f, they have been set such that a group of 2×3 unit cells are translationnaly symmetric.

In this paper, we are interested in working with the minimum period of the problem in order to reduce the computation cost as far as possible. Using the smallest cell has also the advantage to avoid curve folding phenomena, simplifying the interpretation of dispersion curves [30]. The contribution of this paper lies in the analysis of bi-helical periodic configurations, exploiting the smallest unit cell, such that: $\phi_\alpha \notin \{0, \pm\pi/2\}$, $N_1 \neq N_2$ and $N_1L_2/N_2L_1 \neq \pm 1$.

Note that in Fig. 2, the helices of Layer **1** and Layer **2** have been defined on the same cylindrical surface $R_1 = R_2$ (typically, the mid-surface of the structure). However, the helices can be defined on two different cylindrical surfaces, $R_1 \neq R_2$, which can be convenient depending on the problem (typically, when Layer **1** and **2** are physical – see example in Sec. 7).

3. Bi-helical coordinate system

In this section, a natural curvilinear coordinate system attached to the bi-helical geometry of the problem is built. The properties of this system regarding Bloch waves are discussed. For an introduction to the use of general curvilinear coordinate systems, tensor calculus and differential geometry, the reader may refer to Refs. [39, 40, 41] for instance.

3.1. Definition of the coordinate system

The coordinates of the system have to map the helical geometry of both layers. As shown in Fig. 2, the first coordinate s_1 is curvilinear and follows the helices of Layer **1**, while the second coordinate s_2 is also curvilinear but follows the helices of Layer **2**.

The helical direction s_1 and s_2 can be linearly related to the cylindrical coordinates θ and z as follows:

$$z = \frac{L_1}{l_1}s_1 + \frac{L_2}{l_2}s_2 \tag{2a}$$

$$\theta = \frac{2\pi}{l_1}s_1 + \frac{2\pi}{l_2}s_2 \tag{2b}$$

or inversely:

$$s_1 = \frac{l_1L_2}{2\pi(L_2 - L_1)}\theta - \frac{l_1}{L_2 - L_1}z \tag{3a}$$

$$s_2 = -\frac{l_2L_1}{2\pi(L_2 - L_1)}\theta + \frac{l_2}{L_2 - L_1}z \tag{3b}$$

Without loss of generality, the origin $(s_1, s_2) = (0, 0)$ has been arbitrarily set to $(\theta, z) = (0, 0)$ in the above equations.

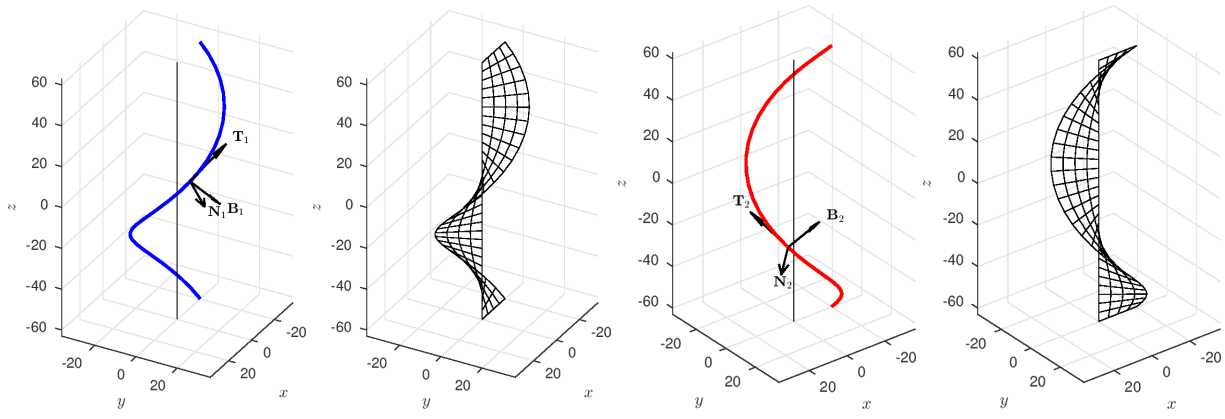

Figure 3: Examples of curves and surfaces with constant coordinates in the bi-helical system: (a) curve (s_2, r)=$(0, R)$, (b) surface s_2=0, (c) curve (s_1, r)=$(0, R)$, (d) surface s_1=0. In this example, the directions s_1 and s_2 are right-handed and left-handed respectively ($\phi_1\phi_2 < 0$) and $R = 20$. Figures (a) and (c) also plot the local Serret-Frenet basis $(\mathbf{N}_\alpha, \mathbf{B}_\alpha, \mathbf{T}_\alpha)$ associated with the curves, which are needed to parametrize the unit cell geometry as detailed in Sec. 3.4.

The last coordinate of the system is chosen as the radial coordinate r of the cylindrical coordinate system, which extends the two-dimensional mapping (s_1, s_2) to three dimensions. The three-dimensional coordinates are hence (s_1, s_2, r). They will be termed as bi-helical coordinates.

As shown in the following, the bi-helical coordinates can be used to represent the position vector $\mathbf{OM}$ of an arbitrary point M in the three-dimensional space. Let us start from the position vector written in the cylindrical system, $\mathbf{OM} = r\mathbf{e}_r(\theta) + z\mathbf{e}_z$ (with $\mathbf{e}_r = \cos\theta\mathbf{e}_x + \sin\theta\mathbf{e}_y$). Using the relationships (2), the position vector $\mathbf{OM} = x\mathbf{e}_x + y\mathbf{e}_y + z\mathbf{e}_z$ in the Cartesian basis can now be written in terms of the bi-helical coordinates (s_1, s_2, r) as:

$$\mathbf{OM} = r\cos\left(\frac{2\pi}{l_1}s_1 + \frac{2\pi}{l_2}s_2\right)\mathbf{e}_x + r\sin\left(\frac{2\pi}{l_1}s_1 + \frac{2\pi}{l_2}s_2\right)\mathbf{e}_y + \left(\frac{L_1}{l_1}s_1 + \frac{L_2}{l_2}s_2\right)\mathbf{e}_z \tag{4}$$

The above equation gives the relationships between the Cartesian coordinates (x, y, z) of any point M in terms of the bi-helical coordinates (s_1, s_2, r).

From Eq. (4), it can be shown that the helical curves s_1 and s_2 are inclined by angles with respect to the z-axis equal to $\tan^{-1}\frac{2\pi r}{L_1}$ and $\tan^{-1}\frac{2\pi r}{L_2}$ respectively. These directions are hence generally not orthogonal to each other. Besides, the angles of s_1 and s_2 increase in absolute value with r (they coincide with the helix lay angles defined in Sec. 2, ϕ_1 and ϕ_2, at $r = R_1$ and $r = R_2$ respectively). The surfaces s_1=constant and s_2=constant are helicoids. Figure 3 illustrates these geometrical considerations.

Without loss of generality, the mapping will be defined in this paper such that (s_1, s_2, r) forms a right-handed basis. Since s_1 and s_2 are always oriented towards increasing values of z, this means that the angle of s_1 with respect to the z-axis must be greater than the angle of s_2 for any r. Therefore, the following condition is required:

$$\frac{1}{L_1} > \frac{1}{L_2} \tag{5}$$

3.2. Covariant/contravariant bases and metric tensor

Let us consider the differential of the position vector, $\mathrm{d}\mathbf{OM} = \mathbf{e}_r\mathrm{d}r + r\mathbf{e}_\theta\mathrm{d}\theta + \mathbf{e}_z\mathrm{d}z$. Replacing $\mathrm{d}\theta$ and $\mathrm{d}z$ thanks to Eqs. (2) and collecting terms in $\mathrm{d}s_1$ and $\mathrm{d}s_2$, the vector $\mathrm{d}\mathbf{OM}$ can be rewritten as:

$$\mathrm{d}\mathbf{OM} = \mathbf{g}_1\mathrm{d}s_1 + \mathbf{g}_2\mathrm{d}s_2 + \mathbf{g}_3\mathrm{d}r \tag{6}$$

where $(\mathbf{g}_1, \mathbf{g}_2, \mathbf{g}_3)$ defines the covariant basis, given by:

$$\mathbf{g}_1 = \frac{2\pi r}{l_1}\mathbf{e}_\theta + \frac{L_1}{l_1}\mathbf{e}_z, \quad \mathbf{g}_2 = \frac{2\pi r}{l_2}\mathbf{e}_\theta + \frac{L_2}{l_2}\mathbf{e}_z, \quad \mathbf{g}_3 = \mathbf{e}_r \tag{7}$$

The covariant basis vectors $\mathbf{g}_1 = \partial\mathbf{OM}/\partial s_1$ and $\mathbf{g}_2 = \partial\mathbf{OM}/\partial s_2$ are tangent to the coordinate curves s_1 and s_2 respectively (as sketched in Fig. 2).

The contravariant basis $(\mathbf{g}^1, \mathbf{g}^2, \mathbf{g}^3)$ is defined from $\mathbf{g}^i \cdot \mathbf{g}_j = \delta^i_j$, yielding:

$$\mathbf{g}^1 = \frac{L_2 l_1}{2\pi r(L_2 - L_1)}\mathbf{e}_\theta - \frac{l_1}{L_2 - L_1}\mathbf{e}_z, \quad \mathbf{g}^2 = -\frac{L_1 l_2}{2\pi r(L_2 - L_1)}\mathbf{e}_\theta + \frac{l_2}{L_2 - L_1}\mathbf{e}_z, \quad \mathbf{g}^3 = \mathbf{e}_r \tag{8}$$

Note that both the covariant and contravariant bases are non-orthogonal.

The calculation of the covariant metric tensor, defined by $(\mathbf{g})_{ij} = \mathbf{g}_i \cdot \mathbf{g}_j$, leads to the following result:

$$\mathbf{g} = \begin{bmatrix} \dfrac{4\pi^2 r^2 + L_1^2}{l_1^2} & \dfrac{4\pi^2 r^2 + L_1 L_2}{l_1 l_2} & 0 \\ \dfrac{4\pi^2 r^2 + L_1 L_2}{l_1 l_2} & \dfrac{4\pi^2 r^2 + L_2^2}{l_2^2} & 0 \\ 0 & 0 & 1 \end{bmatrix} \tag{9}$$

It can be noticed that $\mathbf{g}$ does not depend on s_1 and s_2. An important consequence of this property will be discussed in Sec. 4.1.

3.3. Transformation of vector components

Let us rewrite the expression of the covariant basis (7) and the cylindrical basis as follows:

$$\begin{bmatrix} \mathbf{g}_1 \\ \mathbf{g}_2 \\ \mathbf{g}_3 \end{bmatrix} = \begin{bmatrix} 0 & \frac{2\pi r}{l_1} & \frac{L_1}{l_1} \\ 0 & \frac{2\pi r}{l_2} & \frac{L_2}{l_2} \\ 1 & 0 & 0 \end{bmatrix} \begin{bmatrix} \mathbf{e}_r \\ \mathbf{e}_\theta \\ \mathbf{e}_z \end{bmatrix}, \quad \begin{bmatrix} \mathbf{e}_r \\ \mathbf{e}_\theta \\ \mathbf{e}_z \end{bmatrix} = \begin{bmatrix} \cos\theta & \sin\theta & 0 \\ -\sin\theta & \cos\theta & 0 \\ 0 & 0 & 1 \end{bmatrix} \begin{bmatrix} \mathbf{e}_x \\ \mathbf{e}_y \\ \mathbf{e}_z \end{bmatrix} \tag{10}$$

From these expressions, the covariant basis can be related to the Cartesian basis as:

$$\begin{bmatrix} \mathbf{g}_1 \\ \mathbf{g}_2 \\ \mathbf{g}_3 \end{bmatrix} = \mathbb{J}^{\mathrm{T}} \begin{bmatrix} \mathbf{e}_x \\ \mathbf{e}_y \\ \mathbf{e}_z \end{bmatrix}, \quad \mathbb{J}^{\mathrm{T}} = \begin{bmatrix} -\frac{2\pi r}{l_1}\sin\theta & \frac{2\pi r}{l_1}\cos\theta & \frac{L_1}{l_1} \\ -\frac{2\pi r}{l_2}\sin\theta & \frac{2\pi r}{l_2}\cos\theta & \frac{L_2}{l_2} \\ \cos\theta & \sin\theta & 0 \end{bmatrix} \tag{11}$$

and the metric tensor can be expressed in terms of the Jacobian matrix as $\mathbf{g} = \mathbb{J}^{\mathrm{T}}\mathbb{J}$. According to the definition of the contravariant basis, we also have:

$$\mathbb{I} = \begin{bmatrix} \mathbf{g}_1 \\ \mathbf{g}_2 \\ \mathbf{g}_3 \end{bmatrix} \begin{bmatrix} \mathbf{g}^1 & \mathbf{g}^2 & \mathbf{g}^3 \end{bmatrix} \tag{12}$$

where $\mathbb{I}$ denotes the three-by-three identity matrix. Hence, the transformation matrix between the Cartesian basis and the contravariant one is actually equal to $\mathbb{J}^{-1}$:

$$\begin{bmatrix} \mathbf{g}^1 \\ \mathbf{g}^2 \\ \mathbf{g}^3 \end{bmatrix} = \mathbb{J}^{-1} \begin{bmatrix} \mathbf{e}_x \\ \mathbf{e}_y \\ \mathbf{e}_z \end{bmatrix} \tag{13}$$

Any vector $\mathbf{v}$ can be written in the different bases, Cartesian, covariant or contravariant: $\mathbf{v} = v_x\mathbf{e}_x + v_y\mathbf{e}_y + v_z\mathbf{e}_z = v^1\mathbf{g}_1 + v^2\mathbf{g}_2 + v^3\mathbf{g}_3 = v_1\mathbf{g}^1 + v_2\mathbf{g}^2 + v_3\mathbf{g}^3$. The components (v_x, v_y, v_z) are the Cartesian components, (v^1, v^2, v^3) are

referred to as the contravariant components, and (v_1, v_2, v_3) as the covariant components. Covariant or contravariant components can be transformed to Cartesian components through the Jacobian matrix $\mathbb{J}$ by:

$$\begin{bmatrix} v_x \\ v_y \\ v_z \end{bmatrix} = \mathbb{J} \begin{bmatrix} v^1 \\ v^2 \\ v^3 \end{bmatrix} = \mathbb{J}^{-\mathrm{T}} \begin{bmatrix} v_1 \\ v_2 \\ v_3 \end{bmatrix} \tag{14}$$

For symmetries other than translation, it is noteworthy that Bloch theorem cannot be used in its original form. As discussed hereafter, the above-mentioned transformations will have to be considered for a proper application of Bloch theorem to a vector wave equation.

3.4. Geometrical definition of the three-dimensional unit cell

For a structure which extends periodically along straight directions x and y, the unit cell is easy to define. Denoting as Δl_x and Δl_y the cell lengths in both directions, the unit cell can be delimited by the four planes: $x = 0$, $x = \Delta l_x$, $y = 0$ and $y = \Delta l_y$. However, defining the boundaries of the unit cell with periodicity along curved directions is not as trivial as for straight ones.

3.4.1. Cutting surfaces

Let us denote Δl_1 and Δl_2 the curvilinear lengths of the unit cell in the s_1 and s_2 directions respectively. The cell can be delimited by the boundaries $s_1 = 0$, $s_1 = \Delta l_1$, $s_2 = 0$ and $s_2 = \Delta l_2$, denoted as Γ_1^-, Γ_1^+, Γ_2^- and Γ_2^+ respectively.

The position of any point M on Γ_1^+ and Γ_2^+ can be obtained from Eqs. (4), which yields the following parametric equations for the cutting surfaces:

$$\Gamma_1^+ : \mathbf{OM} = r\cos\left(\frac{2\pi}{l_1}\Delta l_1 + \frac{2\pi}{l_2}s_2\right)\mathbf{e}_x + r\sin\left(\frac{2\pi}{l_1}\Delta l_1 + \frac{2\pi}{l_2}s_2\right)\mathbf{e}_y + \left(\frac{L_1}{l_1}\Delta l_1 + \frac{L_2}{l_2}s_2\right)\mathbf{e}_z, \qquad (s_2, r) \in \mathbb{R}\times\mathbb{R}^+ \tag{15a}$$

$$\Gamma_2^+ : \mathbf{OM} = r\cos\left(\frac{2\pi}{l_1}s_1 + \frac{2\pi}{l_2}\Delta l_2\right)\mathbf{e}_x + r\sin\left(\frac{2\pi}{l_1}s_1 + \frac{2\pi}{l_2}\Delta l_2\right)\mathbf{e}_y + \left(\frac{L_1}{l_1}s_1 + \frac{L_2}{l_2}\Delta l_2\right)\mathbf{e}_z, \qquad (s_1, r) \in \mathbb{R}\times\mathbb{R}^+ \tag{15b}$$

The parametric equations for Γ_1^- and Γ_2^- are obtained by replacing Δl_1 and Δl_2 with zero in Eq. (15a) and Eq. (15b) respectively. An example of cutting surfaces is given in Fig. 4a-b. As can be observed, the cutting surfaces $\Gamma_1^\pm$ and $\Gamma_2^\pm$ are helicoids and are hence non-plane, which complicates the parametrization of the geometry of the unit cell.

3.4.2. Local helical coordinate systems

Local coordinate systems attached to the helices can be built from their Serret-Frenet basis. The Serret-Frenet basis of the i-th helix of Layer α, denoted as $(\mathbf{T}_\alpha^{(i)}, \mathbf{N}_\alpha^{(i)}, \mathbf{B}_\alpha^{(i)})$, is defined by the Serret-Frenet formula [41]: $\mathbf{T}_\alpha^{(i)} = \mathrm{d}\mathbf{R}_\alpha^{(i)}/\mathrm{d}s_\alpha$, $\mathrm{d}\mathbf{T}_\alpha^{(i)}/\mathrm{d}\mathbf{s}_\alpha = -\kappa_\alpha \mathbf{N}_\alpha^{(i)}$, $\mathbf{B}_\alpha^{(i)} = \mathbf{T}_\alpha^{(i)} \wedge \mathbf{N}_\alpha^{(i)}$, where $\kappa_\alpha = 4\pi^2 R_\alpha / l_\alpha$ denotes the helix curvature of Layer α. The Serret-Frenet formula yield:

$$\begin{aligned}
\mathbf{N}_\alpha^{(i)}(s_\alpha) &= \cos(2\pi\frac{s_\alpha}{l_\alpha} + \theta_\alpha^{(i)})\mathbf{e}_x + \sin(2\pi\frac{s_\alpha}{l_\alpha} + \theta_\alpha^{(i)})\mathbf{e}_y \\
\mathbf{B}_\alpha^{(i)}(s_\alpha) &= -\frac{L_\alpha}{l_\alpha}\sin(2\pi\frac{s_\alpha}{l_\alpha} + \theta_\alpha^{(i)})\mathbf{e}_x + \frac{L_\alpha}{l_\alpha}\cos(2\pi\frac{s_\alpha}{l_\alpha} + \theta_\alpha^{(i)})\mathbf{e}_y - \frac{2\pi R_\alpha}{l_\alpha}\mathbf{e}_z \\
\mathbf{T}_\alpha^{(i)}(s_\alpha) &= -\frac{2\pi R_\alpha}{l_\alpha}\sin(2\pi\frac{s_\alpha}{l_\alpha} + \theta_\alpha^{(i)})\mathbf{e}_x + \frac{2\pi R_\alpha}{l_\alpha}\cos(2\pi\frac{s_\alpha}{l_\alpha} + \theta_\alpha^{(i)})\mathbf{e}_y + \frac{L_\alpha}{l_\alpha}\mathbf{e}_z
\end{aligned} \tag{16}$$

As an example, Figs. 3a and 3c depict the serret-Frenet basis for a helix in Layer **1** and Layer **2** respectively. A local coordinate system, $(x_\alpha^{(i)}, y_\alpha^{(i)}, s_\alpha)$, associated with the i-th helix of Layer α is then naturally built from the following position vector:

$$\mathbf{OM} = \mathbf{R}_\alpha^{(i)}(s_\alpha) + x_\alpha^{(i)}\mathbf{N}_\alpha^{(i)}(s_\alpha) + y_\alpha^{(i)}\mathbf{B}_\alpha^{(i)}(s_\alpha) \tag{17}$$

The geometrical shape of the structure is usually parametrized from the local coordinate systems because the plane $(x_\alpha^{(i)}, y_\alpha^{(i)})$ is normal to the helix. For instance, a wire of rectangular cross-section (along the i-th helix of Layer α) corresponds to the parametrization $(x_\alpha^{(i)}, y_\alpha^{(i)}, s_\alpha) \in [-a, a]\times[-b, b]\times\mathbb{R}$, where a and b are the cross-section dimensions. A circular wire is parametrized by $(x_\alpha^{(i)}, y_\alpha^{(i)}, s_\alpha) = (\varrho\cos\varphi, \varrho\sin\varphi, s_\alpha)$, with parameters $(\varrho, \varphi, s_\alpha) \in [0, a]\times[0, 2\pi]\times\mathbb{R}$ where a is the cross-section radius.

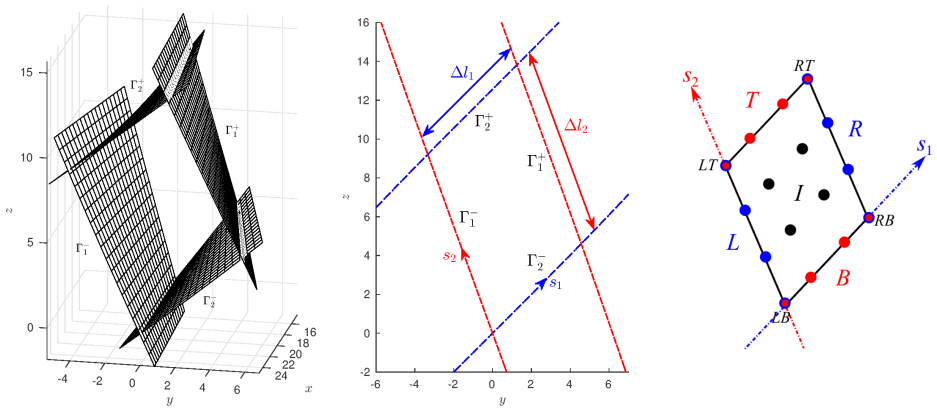

(a) (b) (c)

Figure 4: Cutting surfaces of the unit cell, Γ_1^- ($s_1 = 0$), Γ_1^+ ($s_1 = \Delta l_1$), Γ_2^- ($s_2 = 0$), Γ_2^+ ($s_2 = \Delta l_2$). (a) Three-dimensional view, (b) two-dimensional view, (c) classification of the boundaries of the unit cell into left (L), right (R), bottom (B), top (T) boundaries excluding the four corners LB, RB, LT, RT (the remaining part of the unit cell is the internal (I) region, bullets represent FE nodes). In this example, the directions s_1 and s_2 are right-handed and left-handed respectively ($\phi_1\phi_2 < 0$).

3.4.3. Boundaries of the unit cell

The geometry of the unit cell can be determined by finding the boundaries corresponding to the intersection of the cutting surfaces of Sec. 3.4.1 with the volume parametrization defined from the local systems in Sec. 3.4.2. This is done by equating Eq. (15a) and Eq. (15b) with Eq. (17) written for $\alpha = 1$ and 2 respectively. An example is detailed in Sec. 7 for a complex structure.

3.4.4. Lengths of the unit cell

The curvilinear lengths Δl_1 and Δl_2 of the unit cell, defined on $r = R_1$ and $r = R_2$ respectively, have not yet been determined. Let us determine Δl_2, the curvilinear distance along s_2. In Layer **1**, the boundary $s_2 = 0$ coincides with the helix of zero phase angle, *i.e.* the helix $i = 1$ (of phase $\theta_1^{(1)} = 0$). Then it can be seen from Fig. 2 that the boundary $s_2 = \Delta l_2$ coincides with the helix $i = N_1$, which is of phase angle $\theta_1^{(N_1)}$. One recalls that the helix phase angles are given in the $z = 0$ plane (see Eq. (1)). Hence for $z = 0$ and $\theta = \theta_1^{(N_1)} - \theta_1^{(1)} = -2\pi/N_1$, Eq. (3b) leads to: $s_2 = \Delta l_2 = \frac{l_2}{N_1}\frac{L_1}{L_2 - L_1}$. Similarly, the curvilinear length Δl_1 along s_1 is obtained by setting $z = 0$ and $\theta = \theta_2^{(2)} - \theta_2^{(1)} = 2\pi/N_2$ in Eq. (3a).

Finally, the curvilinear lengths of the unit cell in both directions are:

$$\Delta l_1 = \frac{l_1}{N_2}\frac{L_2}{L_2 - L_1}, \quad \Delta l_2 = \frac{l_2}{N_1}\frac{L_1}{L_2 - L_1} \tag{18}$$

Both curvilinear cell lengths Δl_1 and Δl_2 are always positive thanks to condition (5).

3.5. Particular cases of periodicity

Depending on the geometrical parameters, translational or rotational symmetry can occur by grouping several unit cells. It is instructive to highlight when these kinds of symmetry occur in order to evaluate their computational cost compared with the proposed approach, which exploits the minimum period.

3.5.1. Periodicity by translation

Let us consider the corners of the unit cell, denoted as LB, RB, LT and RT, as depicted by Fig. 4c. Periodicity by translation occurs when opposite corners of the unit cell, that is to say the corners LB and RT, or the corners RB and LT, are aligned along the z-direction. The corners LB and RT will be aligned if $\theta_B + \theta_R = 0$, where θ_B and θ_R are the circumferential angles of the cell boundaries B and R respectively (see also Fig. 4c). Similarly, the corners RB and LT

will be aligned if $\theta_B = \theta_L$. Gathering both possibilities of alignment and noticing that $\theta_R = \theta_L$, the unit cell will thus obey a periodicity by translation if $\theta_B \pm \theta_L = 0$. More generally, the problem will remain periodic by translation for a group of $m_1 \times m_2$ unit cells if:

$$m_1\theta_B \pm m_2\theta_L = 0 \tag{19}$$

From Eq. (15a), it can be inferred that $\theta_B = 2\pi\Delta l_1/L_1$, and from Eq. (15b), $\theta_L = 2\pi\Delta l_2/L_2$. Using Eqs. (18) into (19), a group of $m_1 \times m_2$ unit cells will hence be periodic by translation if:

$$\frac{N_1 L_2}{N_2 L_1} = \mp\frac{m_2}{m_1} \tag{20}$$

The problem will hence have a periodicity by translation if N_1L_2/N_2L_1 is a rational number.

3.5.2. Periodicity by rotation

Periodicity by rotation occurs when opposite corners of the unit cell are aligned along the circumferential θ-direction. This will occur if $z_B = z_L$, where z_B and z_L are the height of the cell boundaries B and L respectively. More generally, the problem will remain periodic by rotation for a group of $m_1 \times m_2$ unit cells if $m_1 z_B = m_2 z_L$. From Eqs. (15a) and (15b), one has $z_B = L_1\Delta l_1/l_1$ and $z_L = L_2\Delta l_2/l_2$. Therefore, the condition for a group of $m_1 \times m_2$ unit cells to be periodic by rotation is:

$$\frac{N_1}{N_2} = \frac{m_2}{m_1} \tag{21}$$

The problem will have a rotational periodicity of order n if the rational number N_1/N_2 is reducible by a factor n.

4. On the consideration of two-dimensional Bloch waves in helical directions

Bloch wave modes can be viewed as waves traveling to infinity without reflection (progressive waves). The condition for such waves to exist is that the problem must be space-periodic. If the geometry is arbitrarily curved, the periodicity is broken and Bloch waves no longer exist. The periodicity can yet be preserved for some particular cases of curvature/torsion of the geometry. The goal of this subsection is to justify the existence of two-dimensional Bloch waves in bi-helical structures, as well as the method to compute these waves considering the vector wave equation of elastodynamics.

4.1. Existence

By definition, a two-dimensional periodic wave problem in the directions (s_1, s_2) is governed by a set of partial differential equations whose coefficients, concatenated in a vector $\mathbf{a}(x, y, s)$, are $(\Delta l_1, \Delta l_2)$-periodic in (s_1, s_2): $\mathbf{a}(s_1 + m_1\Delta l_1, s_2 + m_2\Delta l_2, r) = \mathbf{a}(s_1, s_2, r)$, $\forall(m_1, m_2) \in \mathbb{N}^2$. Then owing to Bloch theorem, there exists wave mode solutions of the form: $\psi(s_1, s_2, r) = \mathrm{e}^{\mathrm{i}(k_1 s_1 + k_2 s_2)} u(s_1, s_2, r; k_1, k_2)$, where (k_1, k_2) are the two-dimensional wavenumbers and u is a $(\Delta l_1, \Delta l_2)$-periodic function in (s_1, s_2) [42, 14].

First, let us assume that the directions (s_1, s_2) are straight. Obviously, The coefficients of the governing equations (including boundary conditions) are periodic if:

1. the material properties are $(\Delta l_1, \Delta l_2)$-periodic,
2. the geometrical shape of the structure is $(\Delta l_1, \Delta l_2)$-periodic.

However, these two conditions are no longer sufficient if periodicity occurs along curved directions. The equilibrium equations have to be written in an appropriate curvilinear coordinate system capable of tracking the geometry of the structure (so that condition 2 can be satisfied). The consequence of this change of coordinate system is that the coefficients of the partial differential equations become also dependent on the so-called Christoffel symbols, related to the geometry. The Christoffel symbols, denoted as Γ^k_{ij}, are defined as follows [41]:

$$\Gamma^k_{ij} = \frac{\partial \mathbf{g}_i}{\partial x^j} \cdot \mathbf{g}^k \tag{22}$$

If the Christoffel symbols do not depend on (s_1, s_2), the periodicity of coefficients in the equilibrium equation will be preserved (provided that the two above-mentioned conditions are also fulfilled), so that Bloch theorem will remain applicable along these curved directions.

Actually, the Christoffel symbols can be expressed as a function of the metric tensor solely by [41]:

$$\Gamma^k_{ij} = \frac{1}{2} g^{kl} \left(\frac{\partial g_{jl}}{\partial x^i} + \frac{\partial g_{il}}{\partial x^j} - \frac{\partial g_{ij}}{\partial x^l} \right) \tag{23}$$

where $g^{ij} = \mathbf{g}^i \cdot \mathbf{g}^j$ is the contravariant metric tensor, equal to the inverse of the covariant metric tensor ($g^{ij} = (\mathbf{g}^{-1})_{ij}$). Therefore, Bloch waves will be supported in the curved directions (s_1, s_2) if $\mathbf{g}$ does not depend on these coordinates. As already noticed from Eq. (9), the independence of $\mathbf{g}$ on (s_1, s_2) is fulfilled by the bi-helical coordinate system. The existence of two-dimensional Bloch waves in helical directions is hence justified, somehow *a posteriori*, from the calculation of the metric tensor.

Note that other kinds of helical coordinate systems have been proposed in the literature [43]. Contrary to the bi-helical system defined in the present paper, these coordinates systems are orthogonal but their metric tensors depend on the three coordinates.

4.2. Vector wave equation

Let us go further by examining the equilibrium equation of elastodynamics, written in a vectorial form: $\nabla \cdot \boldsymbol{\sigma} + \rho\omega^2 \mathbf{u} = \mathbf{0}$, where $\boldsymbol{\sigma} = \mathbf{C} : \boldsymbol{\epsilon}$ is the stress tensor, $\boldsymbol{\epsilon} = 1/2(\nabla \mathbf{u} + \nabla \mathbf{u}^{\mathrm{T}})$ is the strain tensor and $\mathbf{u}$ is the displacement vector (ρ denotes mass density, ω is the angular frequency, $\mathbf{C}$ is the tensor of material properties). The periodicity of the problem along curved directions imposes to write these equations in a curvilinear coordinate system, yielding tensorial equations of the following form (see *e.g.* Refs. [39, 40, 44, 45]):

$$\sigma^{ij}_{,j} + \Gamma^i_{mj}\sigma^{mj} + \Gamma^j_{mj}\sigma^{im} + \rho\omega^2 g^{ij} u_j = f^i, \quad \sigma^{ij} = C^{ijkl}\epsilon_{kl}, \quad \epsilon_{kl} = \frac{1}{2}(u_{k,l} + u_{l,k} - \Gamma^m_{kl} u_m) \tag{24}$$

where the subscripts $i, j = 1, 2, 3$ are associated with the coordinates s_1, s_2 and r respectively. Subscripts and superscripts denote covariant and contravariant components respectively. Einstein summation convention has been used together with commas for partial derivatives with respect to the coordinates. It can be noticed that the coefficients of the equilibrium equations expressed in the curvilinear coordinate system depend on the Christoffel symbols (in addition to the material properties ρ and C^{ijkl}). As explained previously, since Γ^k_{ij} does not depend on s_1 and s_2, Bloch theorem remains applicable.

Equations (24) are instructive because they clearly indicate that tensor and vector wavefields are written in the covariant or contravariant bases. If other bases are used, there is no guarante that the coefficients of the partial differential equations will remain independent on s_1 ans s_2 (in particular, the Cartesian basis cannot be used). In practice, expressing Eqs. (24) in the bi-helical coordinate system is tedious. Fortunately, there is no need to write these equations with the WFEM, which only requires a special treatment of the boundary conditions (see Sec. 5).

4.3. Remark: projection of vectors in the cylindrical basis

Equation (10) shows that the transformation matrix between the covariant basis and the cylindrical basis does not depend on s_1 and s_2 either. This also holds for the contravariant basis. If the tensorial equations given by Eqs. (24) are rewritten in terms of cylindrical components, the coefficients of the so-obtained partial differential equations will also remain independent of s_1 and s_2. Therefore, Bloch theorem still holds if vector fields are expressed in the cylindrical basis instead of the covariant/contravariant bases. This result constitutes a theoretical justification of the revised boundary conditions proposed in Ref. [30], where the cylindrical basis has been proposed to express periodicity with two discrete screw symmetries.

For any vector $\mathbf{v}$ in the cylindrical basis, $\mathbf{v} = v_r \mathbf{e}_r + v_\theta \mathbf{e}_\theta + v_z \mathbf{e}_z$, we have the following transformation matrix:

$$\begin{bmatrix} v_x \\ v_y \\ v_z \end{bmatrix} = \hat{\mathbb{J}} \begin{bmatrix} v_r \\ v_\theta \\ v_z \end{bmatrix}, \quad \hat{\mathbb{J}} = \begin{bmatrix} \cos\theta & -\sin\theta & 0 \\ \sin\theta & \cos\theta & 0 \\ 0 & 0 & 1 \end{bmatrix} \tag{25}$$

where $\hat{\mathbb{J}}^{-1} = \hat{\mathbb{J}}^T$ (the cylindrical basis is orthonormal).

5. Wave finite element method in the bi-helical system

A time harmonic $e^{-i\omega t}$ dependence of wavefields is assumed. The unit cell of the periodic structure is discretized by the conventional FE method, which leads to the following equation of motion:

$$(\mathbf{K} - \omega^2\mathbf{M} - i\omega\mathbf{C})\mathbf{U} = \mathbf{F} \tag{26}$$

where $\mathbf{K}$, $\mathbf{M}$ and $\mathbf{C}$ are the stiffness, mass and viscous damping symmetric matrices. The vectors $\mathbf{U}$ and $\mathbf{F}$ contain the components of the nodal displacements and forces expressed in the Cartesian basis. As is commonly done with the two-directional WFEM [46, 12, 47], these vectors are partitionned into left (L), right (R), bottom (B), top (T), internal (I) degrees of freedom (dofs), as well as four corners dofs (LB, RB, LT, RT):

$$\mathbf{U} = \begin{bmatrix} \mathbf{U}_{LB} \\ \mathbf{U}_{RB} \\ \mathbf{U}_{LT} \\ \mathbf{U}_{RT} \\ \mathbf{U}_{L} \\ \mathbf{U}_{R} \\ \mathbf{U}_{B} \\ \mathbf{U}_{T} \\ \mathbf{U}_{I} \end{bmatrix}, \quad \mathbf{F} = \begin{bmatrix} \mathbf{F}_{LB} \\ \mathbf{F}_{RB} \\ \mathbf{F}_{LT} \\ \mathbf{F}_{RT} \\ \mathbf{F}_{L} \\ \mathbf{F}_{R} \\ \mathbf{F}_{B} \\ \mathbf{F}_{T} \\ \mathbf{0} \end{bmatrix} \tag{27}$$

As depicted in Fig. 4c, right and left dofs are linked through periodicity in the first direction s_1 while top and bottom dofs are linked through periodicity in the second direction s_2. In the purpose of computing wave modes (free response), one assumes that no external force is applied so that $\mathbf{F}_I = \mathbf{0}$.

5.1. Projection of vector fields

As highlighted in Sec. 4, Bloch theorem involving curved directions of periodicity holds if the vector wavefields are projected in the bases of the curvilinear coordinate system following the geometry of the problem. Therefore, the Cartesian dofs of $\mathbf{U}$ and $\mathbf{F}$ must be transformed into contravariant/covariant components. From Eq. (14), let us denote $\mathbf{J}$ the transformation matrix from the contravariant components to the Cartesian components $\mathbf{U}$. The matrix $\mathbf{J}$ is block diagonal and comprises the three-by-three sub-matrices $\mathbb{J}$ as defined by Eq. (14).

Alternatively, the Cartesian dofs can instead be transformed into cylindrical components as noticed in Sec. 4.3. In this case, one has just to replace $\mathbb{J}$ with $\hat{\mathbb{J}}$ (the matrix $\mathbf{J}$ comprises the three-by-three sub-matrices $\hat{\mathbb{J}}$ as defined by Eq. (25)).

Two approaches can be considered. As done in Refs. [26, 27], the projection of vectors can be applied to the global stiffness and mass matrices of the unit cell. However, it is not necessary to apply it to the internal nodes of the cell. In Refs. [24, 25, 30], the projection of vectors has been applied to the periodic boundary conditions only, keeping the Cartesian coordinate system in the FE formulation of the problem. The present paper follows this second approach.

Partitioning the matrix $\mathbf{J}$ with the same notations as introduced previously for $\mathbf{U}$, the periodic boundary conditions for the nodal displacements are given in covariant components (or alternatively in cylindrical components) by:

$$\mathbf{J}_R^{\mathrm{T}}\mathbf{U}_R = \lambda_1\mathbf{J}_L^{\mathrm{T}}\mathbf{U}_L, \quad \mathbf{J}_T^{\mathrm{T}}\mathbf{U}_T = \lambda_2\mathbf{J}_B^{\mathrm{T}}\mathbf{U}_B \tag{28a}$$

$$\mathbf{J}_{RB}^{\mathrm{T}}\mathbf{U}_{RB} = \lambda_1\mathbf{J}_{LB}^{\mathrm{T}}\mathbf{U}_{LB}, \quad \mathbf{J}_{LT}^{\mathrm{T}}\mathbf{U}_{LT} = \lambda_2\mathbf{J}_{LB}^{\mathrm{T}}\mathbf{U}_{LB}, \quad \mathbf{J}_{RT}^{\mathrm{T}}\mathbf{U}_{RT} = \lambda_1\lambda_2\mathbf{J}_{LB}^{\mathrm{T}}\mathbf{U}_{LB} \tag{28b}$$

with:

$$\lambda_1 = \exp(ik_1\Delta l_1), \quad \lambda_2 = \exp(ik_2\Delta l_2) \tag{29}$$

which defines the wavenumbers k_1 and k_2. These wavenumbers are given in the first Brillouin zone:

$$k_1 \in \left[-\frac{\pi}{\Delta l_1}, \frac{\pi}{\Delta l_1}\right], \quad k_2 \in \left[-\frac{\pi}{\Delta l_2}, \frac{\pi}{\Delta l2}\right] \tag{30}$$

Similarly, the periodic boundary conditions for the nodal forces [46] are given in contravariant components (or alternatively in cylindrical components) by:

$$\mathbf{J}_R^{-1}\mathbf{F}_R + \lambda_1\mathbf{J}_L^{-1}\mathbf{F}_L = 0, \quad \mathbf{J}_T^{-1}\mathbf{F}_T + \lambda_2\mathbf{J}_B^{-1}\mathbf{F}_B = 0 \tag{31a}$$

$$\mathbf{J}_{RT}^{-1}\mathbf{F}_{RT} + \lambda_1\mathbf{J}_{LT}^{-1}\mathbf{F}_{LT} + \lambda_2\mathbf{J}_{RB}^{-1}\mathbf{F}_{RB} + \lambda_1\lambda_2\mathbf{J}_{LB}^{-1}\mathbf{F}_{LB} = 0 \tag{31b}$$

The conditions (28) and (31) can be rewritten under matrix forms as follows:

$$\mathbf{U} = \mathbf{A}\tilde{\mathbf{U}}, \quad \mathbf{B}\mathbf{F} = \mathbf{0} \tag{32}$$

with the notations:

$$\mathbf{A} = \begin{bmatrix} \mathbf{I} & \mathbf{0} & \mathbf{0} & \mathbf{0} \\ \lambda_1\mathbf{J}_{RB}^{-\mathrm{T}}\mathbf{J}_{LB}^{\mathrm{T}} & \mathbf{0} & \mathbf{0} & \mathbf{0} \\ \lambda_2\mathbf{J}_{LT}^{-\mathrm{T}}\mathbf{J}_{LB}^{\mathrm{T}} & \mathbf{0} & \mathbf{0} & \mathbf{0} \\ \lambda_1\lambda_2\mathbf{J}_{RT}^{-\mathrm{T}}\mathbf{J}_{LB}^{\mathrm{T}} & \mathbf{0} & \mathbf{0} & \mathbf{0} \\ \mathbf{0} & \mathbf{I} & \mathbf{0} & \mathbf{0} \\ \mathbf{0} & \lambda_1\mathbf{J}_R^{-\mathrm{T}}\mathbf{J}_L^{\mathrm{T}} & \mathbf{0} & \mathbf{0} \\ \mathbf{0} & \mathbf{0} & \mathbf{I} & \mathbf{0} \\ \mathbf{0} & \mathbf{0} & \lambda_2\mathbf{J}_T^{-\mathrm{T}}\mathbf{J}_B^{\mathrm{T}} & \mathbf{0} \\ \mathbf{0} & \mathbf{0} & \mathbf{0} & \mathbf{I} \end{bmatrix}, \quad \mathbf{B}^{\mathrm{T}} = \begin{bmatrix} \mathbf{I} & \mathbf{0} & \mathbf{0} & \mathbf{0} \\ \lambda_1^{-1}\mathbf{J}_{LB}\mathbf{J}_{RB}^{-1} & \mathbf{0} & \mathbf{0} & \mathbf{0} \\ \lambda_2^{-1}\mathbf{J}_{LB}\mathbf{J}_{LT}^{-1} & \mathbf{0} & \mathbf{0} & \mathbf{0} \\ \lambda_1^{-1}\lambda_2^{-1}\mathbf{J}_{LB}\mathbf{J}_{RT}^{-1} & \mathbf{0} & \mathbf{0} & \mathbf{0} \\ \mathbf{0} & \mathbf{I} & \mathbf{0} & \mathbf{0} \\ \mathbf{0} & \lambda_1^{-1}\mathbf{J}_L\mathbf{J}_R^{-1} & \mathbf{0} & \mathbf{0} \\ \mathbf{0} & \mathbf{0} & \mathbf{I} & \mathbf{0} \\ \mathbf{0} & \mathbf{0} & \lambda_2^{-1}\mathbf{J}_B\mathbf{J}_T^{-1} & \mathbf{0} \\ \mathbf{0} & \mathbf{0} & \mathbf{0} & \mathbf{I} \end{bmatrix}, \quad \tilde{\mathbf{U}} = \begin{bmatrix} \mathbf{U}_{LB} \\ \mathbf{U}_L \\ \mathbf{U}_B \\ \mathbf{U}_I \end{bmatrix} \tag{33}$$

For pure propagating waves ($k_1 \in \mathbb{R}$, $k_2 \in \mathbb{R}$), we have $|\lambda_1| = 1$ and $|\lambda_2| = 1$ so that $\mathbf{B}$ is the conjugate transpose of $\mathbf{A}$ ($\mathbf{B} = \mathbf{A}^*$). Using Eq. (32) into Eq. (27) yields:

$$\mathbf{A}^*(\mathbf{K} - \omega^2\mathbf{M} - \mathrm{i}\omega\mathbf{C})\mathbf{A}\tilde{\mathbf{U}} = \mathbf{0} \tag{34}$$

The matrices $\mathbf{A}^*\mathbf{M}\mathbf{A}$ is Hermitian positive definite ($\mathbf{M}$ is real symmetric positive definite). In this paper, the eigensystem (34) is solved based on the implicitly restarted Arnoldi method with the ARPACK library [48]. If no damping is considered, $\mathbf{K}$ is also real symmetric positive (semi-)definite and $\mathbf{C} = 0$ so that the eigenvalue problem leads to positive real eigenvalues ω^2.

5.2. Relationship between propagation constants

As opposed to a plate-like geometry, the propagation constants λ_1 and λ_2 in a structure of cylindrical type are not independent. An important property of the geometry is that the position of any arbitrary point of the structure can be recovered by traveling the distance of N_2 unit cells in the direction s_1 and then traveling back the distance of N_1 unit cells in the direction $-s_2$ (or equivalently, N_1 unit cells in the direction s_2 and N_2 unit cells in the direction $-s_1$). Hence, the following fundamental relationship holds:

$$\lambda_1^{N_2}\lambda_2^{-N_1} = 1 \tag{35}$$

In terms of wavenumbers, this leads to:

$$(k_1\Delta l_1 - 2p_1\pi)N_2 - (k_2\Delta l_2 - 2p_2\pi)N_1 = 2n_\alpha\pi \tag{36}$$

where p_1 and p_2 are integers ensuring that k_1 and k_2 lie in the first Brillouin zone and n_α is an integer corresponding to a user-defined input parameter. As shown further in Sec. 5.3, this integer can be interpreted as a circumferential order.

For a given value of $k_1 \in [-\pi/\Delta l_1, +\pi/\Delta l_1]$ ($p_1 = 0$), k_2 is determined by:

$$k_2 = \frac{k_1\Delta l_1 N_2}{\Delta l_2 N_1} + \frac{2\pi}{\Delta l_2}\left(p_2 - \frac{n_1}{N_1}\right) \tag{37}$$

where p_2 is the integer such that $k_2 \in [-\pi/\Delta l_2, +\pi/\Delta l_2]$. Interestingly, the expression (37) shows that the parameter n_1 can only take N_1 consecutive integer values in the first Brillouin zone, which we will denote $n_1 \in \mathbb{N}_1$ (because the symmetry of our problem is discrete, n_α has to lie inside a finite set).

Alternatively, one can determine k_1 for a given value of $k_2 \in [-\pi/\Delta l_2, +\pi/\Delta l_2]$ ($p_2 = 0$):

$$k_1 = \frac{k_2 \Delta l_2 N_1}{\Delta l_1 N_2} + \frac{2\pi}{\Delta l_1}\left(p_1 + \frac{n_2}{N_2}\right) \tag{38}$$

where p_1 is the integer ensuring that $k_1 \in [-\pi/\Delta l_1, +\pi/\Delta l_1]$. In this case, the integer n_2 can now take N_2 consecutive integer values in the first Brillouin zone, which we will denote $n_2 \in \mathbb{N}_2$.

For the computation of the eigensolutions $\{\omega^2, \tilde{\mathbf{U}}\}$ of Eq. (34), determining k_2 from k_1 or vice-versa is a matter of choice. Yet in practice, the choice leading to the largest set for the circumferential order can help in classifying the modes (see example in Sec. 6.2).

For simplicity in this paper, one will adopt the numbering $\mathbb{N}_\alpha = \{0, 1, ..., N_\alpha - 1\}$ (although it could be more convenient to center the numbering on zero in order to easily pair modes rotating in opposite directions [31]).

5.3. Post-processing the modal properties in the axial direction

The characteristics of wave propagation in the z-direction are of particular interest and have to be post-processed. First, let us remind that the Bloch theory allows expressing any acoustic field ψ at any point $(s_1, s_2, r) = (m_1 \Delta l_1, m_2 \Delta l_2, r)$ from the field at the origin $(0, 0, r)$:

$$\psi(s_1, s_2, r) = \mathrm{e}^{\mathrm{i}(k_1 s_1 + k_2 s_2)} \psi(0, 0, r) \tag{39}$$

where m_1 and m_2 are integers. Using the change of variable given by Eq. (3), the exponential term can be rewritten in terms of the cylindrical coordinates θ and z. The coefficients for θ and z can then be interpreted as k_θ and k_z, the wavenumbers in the θ and z directions respectively, leading to the following expressions:

$$\begin{cases} k_z = \dfrac{k_2 l_2 - k_1 l_1}{L_2 - L_1} \\ k_\theta = \dfrac{k_1 l_1 L_2 - k_2 l_2 L_1}{2\pi(L_2 - L_1)} \end{cases} \tag{40}$$

From Eqs. (18) and (37) or (38), the above expression of k_θ yields:

$$k_\theta = n_\alpha \tag{41}$$

This shows that the parameter n_α can be interpreted as the circumferential order of the problem, n_α varying between N_1 consecutive values or N_2 consecutive values (depending on whether k_1 or k_2 is fixed). This also shows that the condition $\psi(r, \theta + 2\pi, z) = \psi(r, \theta, z)$ is hence automatically fulfilled by the numerical method (the wavefields at the same position but described by θ and $\theta + 2\pi$ are identical).

As far as the group velocity is concerned, its value in the z-direction is defined by $c_g = \frac{\partial \omega}{\partial k_z}$, which yields:

$$c_g = \frac{\partial \omega}{\partial k_1}\frac{\partial k_1}{\partial k_z} + \frac{\partial \omega}{\partial k_2}\frac{\partial k_2}{\partial k_z} \tag{42}$$

Inverting Eq. (40), one gets:

$$\begin{cases} k_1 = \dfrac{2\pi}{l_1} k_\theta + \dfrac{L_1}{l_1} k_z \\ k_2 = \dfrac{2\pi}{l_2} k_\theta + \dfrac{L_2}{l_2} k_z \end{cases} \tag{43}$$

Equation (43) shows that $\frac{\partial k_1}{\partial k_z} = \frac{L_1}{l_1}$ and $\frac{\partial k_2}{\partial k_z} = \frac{L_2}{l_2}$. The group velocity in the z-direction is hence:

$$c_g = \frac{L_1}{l_1} c_{g_1} + \frac{L_2}{l_2} c_{g_2} \tag{44}$$

The expression for c_e, the energy velocity in the z-direction, is obtained by replacing the subscripts g with e in the above expression. The calculation of the group and energy velocities in the helical directions, c_{g_α} and c_{e_α}, is detailed in Appendix A.

6. Validation

In this section, the bi-helical WFEM is validated for two test cases. One assumes isotropic materials without damping. E, ρ and ν denote Young's modulus, mass density and Poisson's ratio respectively. The dispersion curves will be given for the normalized wavenumber $k\ell$ or the normalized group velocity c_g/c as a function of the normalized frequency $\omega\ell/c$, where k is a wavenumber (k_z or k_2), ℓ is a characteristic length and c is a characteristic wave velocity depending on the test case. The Poisson's ratio is set to $\nu = 0.3$.

The three-dimensional FE discretization of the unit cell is generated so that the two-dimensional elements of the right and top boundaries are forced to match those of the left and bottom boundaries respectively (this allows a direct connection of right and top dofs with left and bottom dofs). The FE meshes of this paper have been built from the free software Gmsh [49] using ten-nodes tetrahedral elements (quadratic interpolating functions). The bi-helical WFEM has been implemented in an in-house FE code written in Matlab.

6.1. Uniform tube test case

A homogeneous and uniform tube is considered. The thickness and the mid-surface radius are denoted as h and R respectively. The inner and outer radii are hence equal to $R - h/2$ and $R + h/2$. The characteristic length and wave velocity are chosen as the thickness ($\ell = h$) and the shear wave velocity ($c = c_s = \sqrt{E/2\rho(1+\nu)}$). The symmetry is continuous along both the axial and the circumferential directions. Consequently, the problem can also be artificially viewed as bi-helical along two different helical directions arbitrarily defined.

The volume corresponding to the bi-helical unit cell is parametrized by Eq. (4) with $r \in [R - h/2, R + h/2]$. Its intersection with $\Gamma_1^{\pm}$ is determined by setting $s_1 = 0$ and $s_1 = \Delta l_1$. Since the unit cell is additionally delimited by $\Gamma_2^{\pm}$, one has $s_2 \in [0, \Delta l_2]$. Therefore, the left and right boundaries of the unit cell are parametrized by Eq. (15a) with:

$$(s_2, r) \in [0, \Delta l_2] \times [R - h/2, R + h/2] \tag{45}$$

Similarly, the bottom and top boundaries of the unit cell (intersection with $\Gamma_2^{\pm}$) are parametrized by Eq. (15b) with:

$$(s_1, r) \in [0, \Delta l_1] \times [R - h/2, R + h/2] \tag{46}$$

The following paremeters are set: $R_1 = R_2 = R$, $\phi_1 = 20°$, $\phi_2 = -20°$. The eigenproblem (34) is solved for the eigenvalue ω^2. From the wavenumber k_1 given inside the interval $[-\pi/\Delta l_1, \pi/\Delta l_1]$, the wavenumber k_2 is calculated according to Eq. (37) for various circumferential orders n_1. Two geometries are considered.

For the first one, we set $R/h = 74.5$. This first case can be considered as a thin shell problem and allows a comparison with the analytical solution obtained from Flügge theory [50], recalled in Appendix B. The parameters N_1 and N_2 are set to 110 and 100 respectively. As can be observed in Fig 5a, the periodicity boundaries of the unit cell are almost planar. The dispersion curves are computed for various circumferential orders n_1 and shown in Fig. 5b. Good agreement is found with the analytical solution.

For the second one, we set $R/h = 2$. In this case, the structure is thick and can no longer be approximated as a thin shell. The parameters N_1 and N_2 are set to 40 and 30 respectively. The FE mesh of the unit cell is shown in Fig. 6a. The non-planar nature of the periodic boundaries (left, right, top and bottom), as explained earlier in Sec. 3.4.1, is clearly visible as opposed to the first case, which constitutes a further validation test. The dispersion curves are computed for various circumferential orders n_1 and shown in Fig. 6b.

For both thin and thick problems, the results are compared with those obtained from a straight unit cell, that is to say, cut along the directions θ (circumferential) and z (axial) of the cylindrical coordinate system as is commonly done [26, 27, 28]. The results obtained with the bi-helical approach fully agree in both cases.

Note that the definition of the circumferential order differs from one model to another. In a WFEM model, the circumferential order n_1 is such that $n_1 \in \mathbb{N}_1$. In Flügge theory, the circumferential order n lies in the infinite set of integers ($n \in \mathbb{Z}$). For plotting the results in Figs. 5b and 6b, the parameters n_1 and n are yet identical, which is explained by the fact that the size of the cell and the frequency range considered are both relatively small in these test cases.

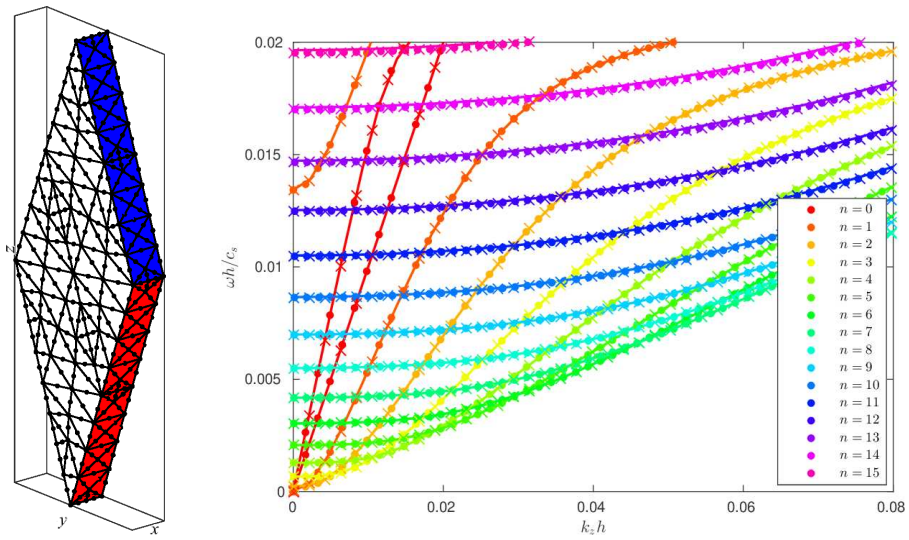

(a) (b)

Figure 5: Thin tube test case ($R/h = 74.5$). (a) FE mesh of the bi-helical unit cell (3198 dofs), (b) normalized dispersion curves for various circumferential orders n, computed with the bi-helical unit cell (•), with a straight unit cell (×) cut along θ and z ($N_\theta = 100$, $\Delta l_z = 3h$) and with Flügge theory (–). Color online.

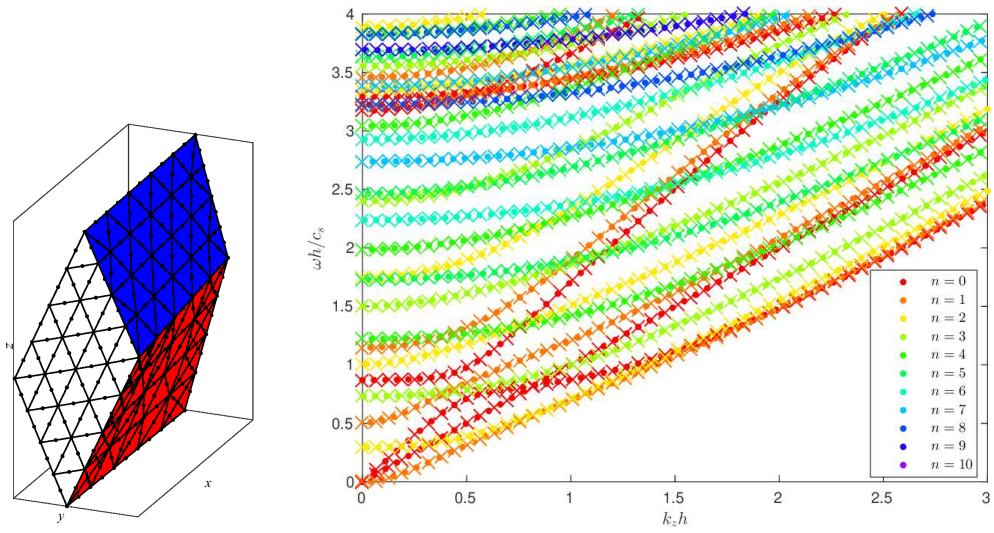

(a) (b)

Figure 6: Thick tube test case ($R/h = 2$). Same legend as Fig. 5 (with 4521 dofs, $N_\theta = 40$, $\Delta l_z = 0.5h$). Color online.

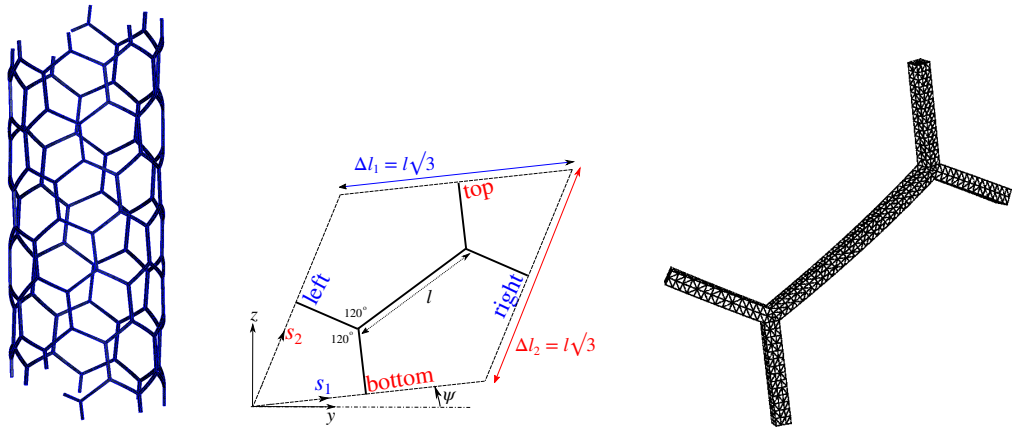

(a) (b) (c)

Figure 7: (a) Nanotube like structure (built with 50 unit cells), (b) parameters of the unit cell and its boundaries, (c) three-dimensional FE mesh of the unit cell (23133 dofs).

6.2. *Chiral nanotube*

The second validation test case concerns a chiral nanotube and is taken from Ref. [30]. The structure is obtained from tilting a hexagonal lattice by a chiral angle ψ and rolling up the lattice around a virtual cylinder of radius R. As illustrated in Fig. 7a, the so-obtained structure is screw symmetric along two directions, *i.e.* bi-helical as defined in this paper.

The chiral angle and the radius are set to $\psi = \arctan\frac{\sqrt{3}}{15}$ and $R = \frac{\sqrt{3}\sqrt{15^2+3}}{4\pi}l$ respectively, where l denotes the side length of the hexagonal lattice. The unit cell of the problem is sketched in Fig. 7b with its helical direction of periodicity, s_1 and s_2. The widths of the unit cell are given by $\Delta l_1 = \Delta l_2 = \sqrt{3}l$. The helical parameters are set as follows:

$$\phi_1 = \frac{\pi}{2} - \psi = \arctan\frac{15}{\sqrt{3}}, \quad \phi_2 = \phi_1 - \frac{\pi}{3} = \arctan\frac{\sqrt{3}}{4}, \quad R_1 = R_2 = R \tag{47}$$

From Eqs. (18), it can be checked that $N_1 = 1$ and $N_2 = 8$. Note that the ratio N_1/N_2 is an irreducible rational number, so that there is no pure periodicity by rotation in this example. The ratio $L_1/L_2 = \tan\phi_2/\tan\phi_1$ is a rational number, which means that there is a periodicity by translation. From Eq. (20), This periodicity occurs for a group of 2×5 unit cells ($N_1L_2/N_2L_1 = 5/2$). Accounting for this symmetry would hence lead to a drastic increase of the problem size by a factor 10.

The beam cross-section of the hexagonal lattice is square with a thickness equal to $2\sqrt{3}l/50$. The FE mesh of the unit cell is shown in Fig. 7c. The structure is meshed with three-dimensional elements in this paper (one-dimensional beam elements have been used in Ref. [30]).

The eigenproblem (34) is solved for the eigenvalue ω^2. From the wavenumber k_2 given inside the interval $[-\pi/\Delta l_2, \pi/\Delta l_2]$, the wavenumber k_1 is calculated according to Eq. (38) for each circumferential order $n_2 \in \mathbb{N}_2$, $\mathbb{N}_2 = \{0, 1, ..., 7\}$.

Figure 8a gives the dispersion curves of the nanotube for the normalized frequency $\omega l/c_0$ as a function of the normalized wavenumber $k_2\Delta l_2$, where $c_0 = \pi^2\sqrt{\frac{E}{\rho}}$. This normalization is chosen similarly to Ref. [30] for a direct comparison of figures. Figure 8a correlates fairly well with that found in [30]. In particular, the bandgap observed around the frequency $\omega l/c_0 \simeq 0.018$ is properly identified. As an additional result in this paper, the normalized group velocity along the z-direction, calculated from Eq. (44), is shown in Fig. 8b. It can be observed that the fastest waves occur for the lowest circumferential order ($n = 0$).

Figure 8 also shows the results if, alternatively, k_1 is fixed inside the interval $[-\pi/\Delta l_1, \pi/\Delta l_1]$ and k_2 is determined according to Eq. (37) for $n_1 = 0$ (since $N_1 = 0$, note that $\mathbb{N}_1 = \{0\}$). As expected, results are identical to those

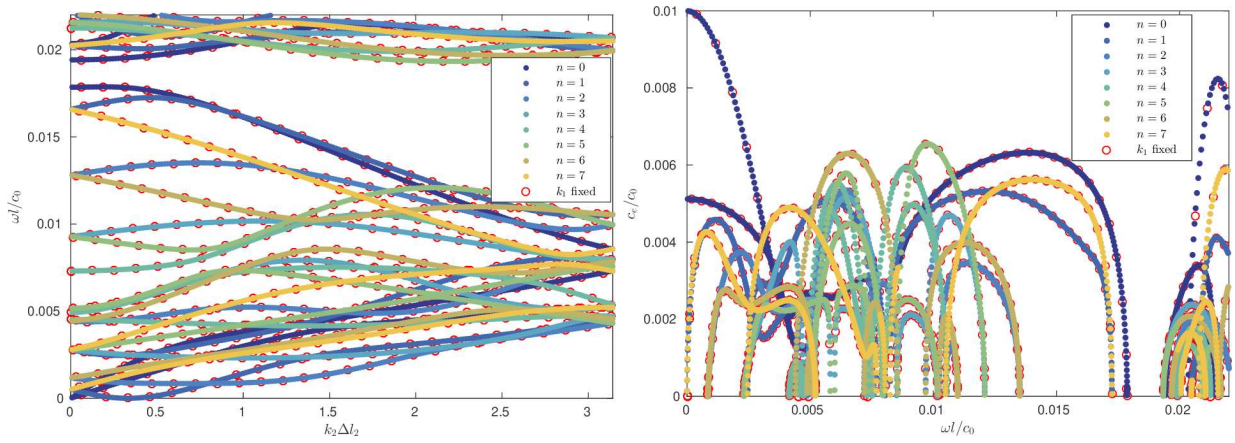

(a) (b)

Figure 8: Dispersion curves for a chiral nanotube calculated by setting $k_2 \in [-\pi/\Delta l_2, \pi/\Delta l_2]$ and $n_2 = 0, 1, ..., 7$ (•) and by setting $k_1 \in [-\pi/\Delta l_1, \pi/\Delta l_1]$ and $n_1 = 0$ (o). (a) Normalized frequency as a function of the wavenumber along the s_2-direction, (b) normalized group velocity along the z-direction as a function of frequency. Color online.

previously obtained. However, this choice does not help to classify the wave modes in terms of the circumferential order because $\mathbb{N}_1$ is a singleton in this example. As rule of thumb, it is hence preferable to fix k_α such that the cardinality of $\mathbb{N}_\alpha$ is the greatest.

7. Application to multi-wire cables

The overall approach proposed in this paper is now applied to investigate wave propagation in a multi-wire bi-helical periodic structure, representing the armor of a cable used in the energy industry. As already explained in Sec. 1, the armor consists of two layers of wires twisted with different angles, which yields a bi-helical periodic media. To simplify the problem and since our attention is focused on this component, only the armor will be modeled, the internal and the external parts of the cable being discarded. In this final example, we are particularly interested in modes propagating predominantly in the individual wires to see how much the double armor structure affects their behavior.

7.1. Geometrical description of the unit cell

The structure consists of two cylindrical layers of helical wires (see Fig. 9). The outer layer, Layer **1**, is formed by N_1 helical wires twisted around the z-axis in the counter-clockwise direction (right-handed, $\phi_1 > 0$). The inner layer, Layer **2**, is formed by N_2 helical wires twisted in the clockwise direction (left-handed, $\phi_2 < 0$). The wire cross-section is circular and will be denoted as a_1 and a_2 in the outer and inner layer respectively.

Inside each layer, it is assumed that there is no interwire contact. However, both layers are separated by a thin intermediate homogeneous cylindrical layer of thickness $h = R_1 - a_1 - (R_2 + a_2)$. Every wire of the structure is in contact with this layer.

The whole geometry of the unit cell has to be created with a FE mesh generator (Gmsh [49], in this paper). As shown in Fig. 9c, the cutting surfaces $\Gamma_1^\pm$ intersect the helical outer wire and the cutting surfaces $\Gamma_2^\pm$ intersect the helical inner wire of the unit cell. $\Gamma_1^\pm$ and $\Gamma_2^\pm$ also intersect the intermediate cylindrical layer. It remains necessary to detail how to parametrize the boundaries of the unit cell in the bi-helical coordinate system, that is to say, the left, right, bottom and top boundaries.

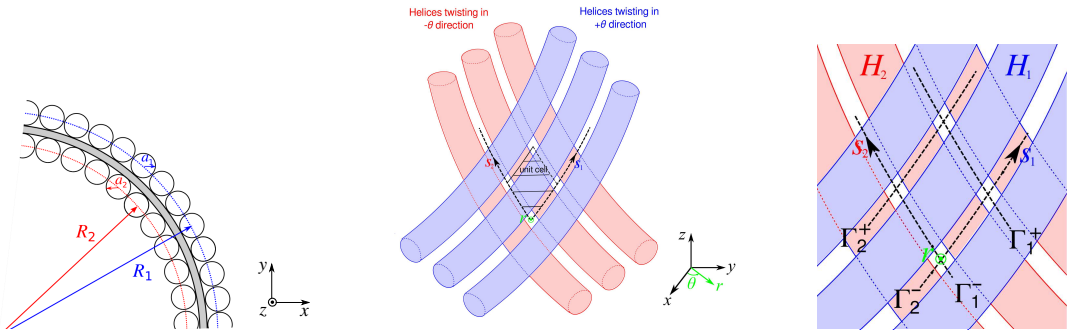

(a) (b) (c)

Figure 9: Skecth of a double armor structure. The wires are helical, twisted around the z-axis. The inner layer (red) is twisted in the direction opposite to the outer layer (blue). Both layers are separated by an intermediate cylindrical layer. (a) Cross-section in the (x, y) plane, (b) front view (without intermediate layer) and unit cell of the structure, (c) definition of volumes and cutting surfaces of the unit cell. Also represented are the different coordinate systems: Cartesian (x, y, z), cylindrical (r, θ, z) and bi-helical (s_1, s_2, r).

7.1.1. Outer wire boundaries (left and right)

Without loss of generality, let us consider the outer wire $i = 1$. Its phase angle $\theta_1^{(1)}$, involved in Eqs. (1) and (16), is zero. Based on the local coordinate system defined in Sec. 3.4.2, the volume of the outer wire, denoted as H_1 in Fig. 9c, is parametrized by the following equation given for any point M inside the volume:

$$\begin{aligned}\mathbf{OM} =& \mathbf{R}_1^{(1)}(s_1) + \varrho_1 \cos\varphi_1 \mathbf{N}_1^{(1)}(s_1) + \varrho_1 \sin\varphi_1 \mathbf{B}_1^{(1)}(s_1) \\ =& \left((R_1 + \varrho_1 \cos\varphi_1)\cos\frac{2\pi s_1}{l_1} - \varrho_1 \frac{L_1}{l_1}\sin\varphi_1 \sin\frac{2\pi s_1}{l_1}\right)\mathbf{e}_x + \\ & \left((R_1 + \varrho_1 \cos\varphi_1)\sin\frac{2\pi s_1}{l_1} + \varrho_1 \frac{L_1}{l_1}\sin\varphi_1 \cos\frac{2\pi s_1}{l_1}\right)\mathbf{e}_y + \\ & \left(\frac{L_1}{l_1}s_1 - \varrho_1 \frac{2\pi R_1}{l_1}\sin\varphi_1\right)\mathbf{e}_z\end{aligned} \tag{48}$$

with $\varrho_1 \in [0, a_1]$, $\varphi_1 \in [0, 2\pi]$ and $s_1 \in \mathbb{R}$. The parameters ϱ_1 and φ_1 can be viewed as the local polar coordinates in the cross-section of the outer wire.

Right and left boundaries of the unit cell are obtained from the intersection between the cutting surfaces $\Gamma_1^{\pm}$ and the volume H_1. They can be found by equating Eqs. (15a) and (48), which allows expressing the variables r and s_2 in terms of ϱ_1, φ_1 and s_1 as:

$$\begin{cases} r^2 = (R_1 + \varrho_1 \cos\varphi_1)^2 + (\varrho_1 \dfrac{L_1}{l_1}\sin\varphi_1)^2 \\ \dfrac{L_2}{l_2}s_2 = \dfrac{L_1}{l_1}s_1 - \varrho_1 \dfrac{2\pi R_1}{l_1}\sin\varphi_1 - \dfrac{L_1}{l_1}\Delta l_1 \end{cases} \tag{49}$$

Thanks to Eqs. (49), r and s_2 can be eliminated from the equality between Eqs. (15a) and (48) in the x-direction, yielding the single equation:

$$\begin{aligned}&(R_1 + \varrho_1 \cos\varphi_1)\cos\frac{2\pi s_1}{l_1} - \varrho_1 \frac{L_1}{l_1}\sin\varphi_1 \sin\frac{2\pi s_1}{l_1} = \\ &\sqrt{(R_1 + \varrho_1 \cos\varphi_1)^2 + (\varrho_1 \frac{L_1}{l_1}\sin\varphi_1)^2}\cos\left(\frac{4\pi^2 R_1}{L_2 l_1}\varrho_1 \sin\varphi_1 - \frac{2\pi L_1}{L_2 l_1}s_1 + (1 + \frac{L_1}{L_2})\frac{2\pi\Delta l_1}{l_1}\right)\end{aligned} \tag{50}$$

This equation gives a relationship between the variables s_1, φ_1 and ϱ_1 and defines the right boundary of the unit cell. The equation for the left boundary is obtained by setting Δl_1 to zero in the above equation. In this paper, this

	R_α/a	ϕ_α	N_α
Layer **1**	40.40	$+20°$	112
Layer **2**	37.89	$-20°$	106

Table 1: Geometrical parameters (thickness of the intermediate layer: $h = 0.51a$).

non-linear equation is solved numerically for s_1 based on a Nelder-Mead simplex algorithm, with $\varrho_1 \in [0, a_1]$ and $\varphi_1 \in [0, 2\pi]$. Once the value of s_1 is found for a specified set of values (ϱ_1, φ_1), the left and right surfaces can be built in the Cartesian coordinate system from Eq. (48). As already mentioned previously, the resulting surface is not planar since the cutting surface are helicoids.

7.1.2. Inner wire boundaries (bottom and top)

The volume of the inner wire $i = 1$, denoted as H_2, is parametrized by an equation identical to Eq. (48) by replacing subscripts 1 with 2:

$$\begin{aligned}\mathbf{OM} = &\left((R_2 + \varrho_2 \cos\varphi_2)\cos\frac{2\pi s_2}{l_2} - \varrho_2\frac{L_2}{l_2}\sin\varphi_2 \sin\frac{2\pi s_2}{l_2}\right)\mathbf{e}_x + \\ &\left((R_2 + \varrho_2 \cos\varphi_2)\sin\frac{2\pi s_2}{l_2} + \varrho_2\frac{L_2}{l_2}\sin\varphi_2 \cos\frac{2\pi s_2}{l_2}\right)\mathbf{e}_y + \\ &\left(\frac{L_2}{l_2}s_2 - \varrho_2\frac{2\pi R_2}{l_2}\sin\varphi_2\right)\mathbf{e}_z\end{aligned} \tag{51}$$

The bottom and top boundaries of the unit cell are the intersection between the cutting surfaces $\Gamma_2^\pm$ and the volume H_2 (see Fig. 9c). The intersection is found by equating Eqs. (15b) and (51), which yields an equation identical to Eq. (50) except that subscripts 1 and 2 have to be switched.

7.1.3. Boundaries of the intermediate cylindrical layer

The volume corresponding to the thin intermediate layer is parametrized by Eq. (4) with $r \in [R_2 + a_2, R_1 - a_1]$. Its intersection with $\Gamma_1^\pm$ is determined by setting $s_1 = 0$ and $s_1 = \Delta l_1$. Since the unit cell is additionally delimited by $\Gamma_2^\pm$, one has $s_2 \in [0, \Delta l_2]$. Therefore, the left and right boundaries of the layer are parametrized by Eq. (15a) with:

$$(s_2, r) \in [0, \Delta l_2] \times [R_2 + a_2, R_1 - a_1] \tag{52}$$

Similarly, the bottom and top boundaries of the layer (intersection with $\Gamma_2^\pm$) are parametrized by Eq. (15b) with:

$$(s_1, r) \in [0, \Delta l_1] \times [R_2 + a_2, R_1 - a_1] \tag{53}$$

7.2. Numerical results

7.2.1. Model parameters

The geometrical parameters chosen for the numerical results are summarized in Table 1. The wire radius is denoted as a and is the same in each layer ($a = a_1 = a_2$). Figures 10a and 10b depict the FE mesh of the unit cell used for the computation in the low-frequency regime (Sec. 7.2.2) and in the high-frequency regime (Sec. 7.2.3) respectively. The periodicity boundaries of the unit cell are almost planar in this case because a is small compared to R_α. Figure 10c shows a reconstitution of the double armor structure built from 10 unit cells along each helical directions, which allows us to check that the unit cell as parametrized from Sec. 7.1 is properly defined from the geometrical point of view.

The wires and the intermediate layer are constituted by a metallic material (steel) and a plastic material (polyethylene) respectively. Both materials are isotropic. The material properties are given in Table 2. Accounting for the viscoelasticity of materials, Young's modulus and Poisson's ratio are complex and given by:

$$E = \rho\tilde{c}_s^2\frac{3\tilde{c}_l^2 - 4\tilde{c}_s^2}{\tilde{c}_l^2 - \tilde{c}_s^2}, \quad \nu = \frac{1}{2}\frac{\tilde{c}_l^2 - 2\tilde{c}_s^2}{\tilde{c}_l^2 - \tilde{c}_s^2} \tag{54}$$

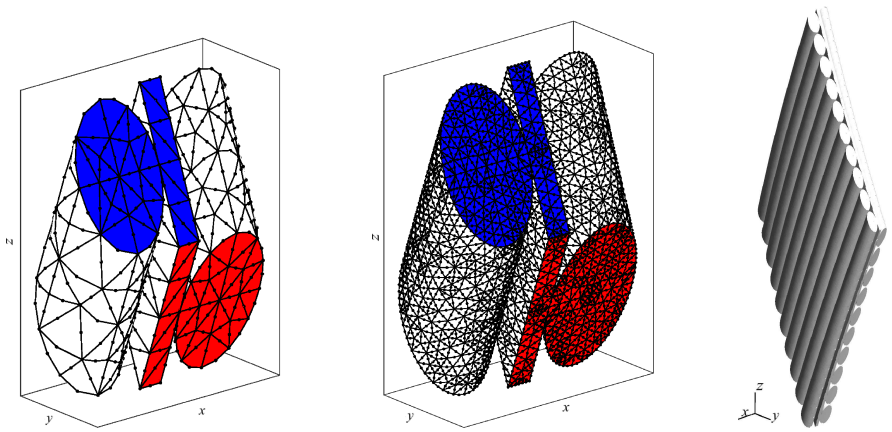

(a) (b) (c)

Figure 10: (a) FE mesh of the unit cell (7374 dofs), (b) FE mesh used in the high-frequency regime (78747 dofs), (c) double armor structure built from 10x10 unit cells.

Material	ρ (kg/m^3)	c_l (m/s)	c_s (m/s)	η_l (Np/wavelength)	η_s (Np/wavelength)
Steel	7800	6020.2	3217.9	0.003	0.008
Polyethylene	1000	1463.9	597.6	0.02	0.16

Table 2: Material properties.

with the complex bulk velocities $\tilde{c}_l$ and $\tilde{c}_s$:

$$\tilde{c}_{l,s} = c_{l,s}\left(1 + \mathrm{i}\frac{\eta_{l,s}}{2\pi}\right)^{-1} \tag{55}$$

where η_l and η_s denote the bulk wave attenuations in Neper per wavelength. No viscous damping is considered ($\mathbf{C} = \mathbf{0}$).

In order to simplify the analysis and reduce the size of the problem, we restrict ourselves to a qualitative study. The FE mesh is not refined near the regions of contact between wires and the intermediate layer. Line contacts are assumed with perfectly stick conditions (no slip, no separation and no friction are considered). The displacement is hence continuous in the three directions along each contact curve (contact curves are helix).

Note that the choice $\phi_2 = -\phi_1$ in Table 1 may seem particular at first sight. However, the helix angles are not defined on the same radius ($R_2 \neq R_1$). The ratio N_1L_2/N_2L_1 is equal to $-R_2N_1/R_1N_2$, where R_2/R_1 is not a rational number (the values given in Table 1 can be viewed as irrationals approximated up to two digits). Hence, there is no pure periodicity by translation in this example. The ratio N_1/N_2 is reducible by a factor 2, so that there is a rotational symmetry of order 2 (which occurs for a group of 53×56 unit cells). Accounting for such a periodicity instead of the bi-helical one would then prohibitively increase the problem size by a factor $53 \times 56 = 2968$.

7.2.2. Low-frequency results

The eigenproblem (34) is solved for ω^2, with k_1 given inside $[-\pi/\Delta l_1, \pi/\Delta l_1]$ and k_2 determined according to Eq. (37). The viscoelasticity of materials is neglected ($\eta_{l,s} = 0$).

Figures 11a and 11b show the dispersion curves computed for the normalized frequency $\omega a/c_s$ as a function of the normalized wavenumber $k_1 a$ for n_1=0 and n_1=5 respectively (here, c_s is the shear wave velocity of steel).

No bandgap is observed. In order to help the identification of wave modes propagating predominantly in wires, Fig. 11c gives the dispersion curves obtained for a free wire, *i.e.* uncoupled from the intermediate layer. In the low-frequency range, four fundamental modes are propagating inside each helical wire: two flexural, one torsional and one longitudinal modes, labeled as F(1,1)$^+$, F(1,1)$^-$, T(0,1) and L(0,1) respectively [24].

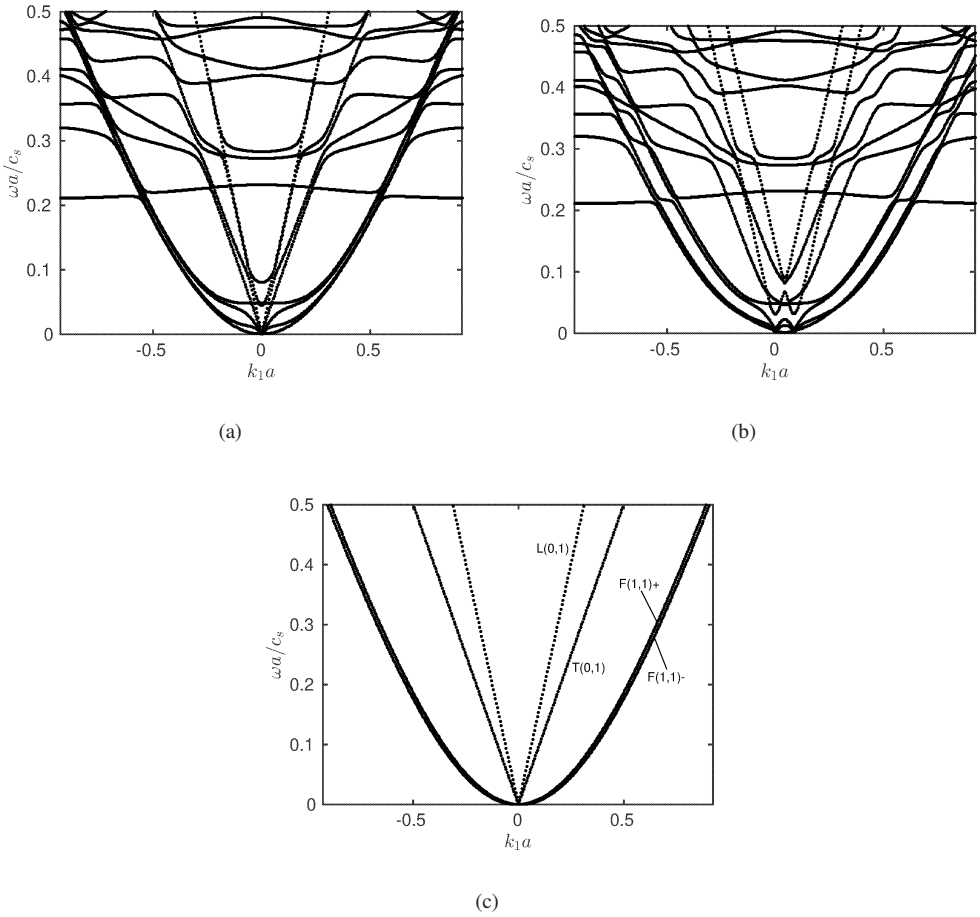

Figure 11: Dispersion curves $\omega a/c_s$ versus $k_1 a$ of the double armor structure for: (a) $n_1 = 0$, (b) $n_1 = 5$. Figure (c): results for a free wire in Layer **1** (wire disconnected from the intermediate layer). The results obtained for a free wire in Layer **2** are nearly identical and not shown.

From Figs. 11a and 11b, the trace of these fundamental modes can still be observed in the double armor structure. This indicates that these modes are moderately perturbed. As usual with weakly coupled systems [51, 52, 53], this perturbation manifests itself as curve veerings (*i.e.* repulsions of modal branches). These veering phenomena can be clearly observed for the T(0,1) mode, which turns out to be more affected by the structural coupling than longitudinal and flexural modes. In addition to these fundamental waves, many other modes can be observed due to the strong coupling of the intermediate layer to the wires.

A closer look at Fig. 11b shows that results are unsymmetric with respect to the frequency axis, which means that modes propagating in opposite directions behave differently. This break of symmetry actually occurs for non-zero circumferential orders, $n_\alpha \neq 0$, and is due to the anisotropy of the structure in the circumferential direction (as similarly found in Ref. [31] with a helical multi-wire geometry).

7.2.3. High-frequency results

Focusing on modes propagating predominantly in the individual wires, the dispersion curves of the double armor structure are now computed in a higher frequency range.

To avoid the computation of too many modes, which would be memory and time-consuming, the eigenvalues in the armor structure are computed around the solutions found preliminarily for a free wire. In practice, this is done with the ARPACK library by specifying a limited number of eigenvalues (here, 20 modes) around a user-defined shift. Besides, viscoelastic properties are introduced (see Table 2) in order to move the complex eigenfrequencies of

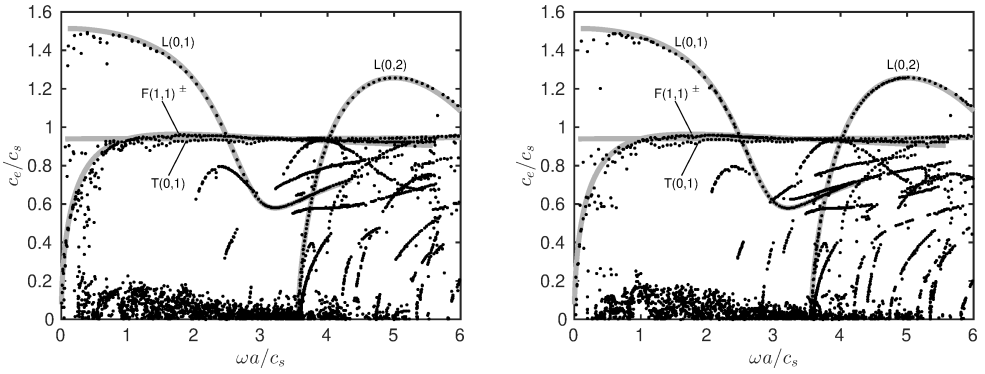

Figure 12: Dispersion curves c_e/c_s as a function of $\omega a/c_s$ of the double armor structure for: (a) $n_1 = 0$, (b) $n_1 = 50$. Results are computed by using an eigenshift obtained from a free wire model. Gray continuous lines: modes of a free wire.

strongly coupled modes, which involve the attenuating intermediate layer and are of little interest, further away from the weakly coupled wire modes.

The eigenproblem (34) is still solved for ω^2, with k_1 fixed to real values and k_2 determined according to Eq. (37). Due to the presence of damping in the system, the eigenfrequencies are now complex-valued. Although it might be preferable from a physical point of view to set the frequency as a fixed real value and look for complex wavenumbers, such a procedure is more complicated to implement [47, 14] and is left out of the scope of this paper. Note that the viscoelastic parameters of Table 2 yet introduce quite small imaginary parts in the material properties, so that the dispersion curves will be negligibly affected by the presence of damping in our results.

Figure 12a gives the dispersion curves for the normalized energy velocity c_e/c_s as a function of the normalized frequency (n_1=0). Also shown are the dispersion curves of the L(0,1), L(0,2), F(1,1)$^{\pm}$ and T(0,1) modes propagating in a free wire. Note that curve veering is more clearly observable on the energy velocity, because it is (approximately) equal to the slope in Fig. 11a (that is to say, the group velocity). Veering mainly occurs in the low-frequency regime of the double armor structure, roughly below $\omega a/c_s \simeq 1$. Above the frequency $\omega a/c_s \simeq 1$, the modes propagating in a free wire are almost unchanged. This shows that these modes tend to propagate freely in the armor structure as the frequency increases. This is confirmed by the results computed for the higher order L(0,2) mode, which turns out to be negligibly affected by the double armor structure.

In Fig. 12a, the solutions of low energy velocity (c_e/c_s<0.2) mainly correspond to waves involving the motion of the intermediate layer (of less interest here). The remaining curves, found for $\omega a/c_s > 2$ and 0.2<c_e/c_s<1, mainly correspond to higher order modes of flexural type propagating predominantly in wires and have not been labeled.

Finally, Fig. 12b shows the dispersion curves computed for a high circumferential order (n_1=50). The interpretation of results is similar to those previously obtained for n_1=0. It is noteworthy that above $\omega a/c_s \simeq 1$, the L(0,1), L(0,2), F(1,1)$^{\pm}$ and T(0,1) curves are nearly identical to Fig. 12a, which further confirms that waves in wires tend to behave freely as the frequency increases.

8. Conclusions

In this paper, the propagation of two-dimensional elastic Bloch waves in helical periodic structures has been investigated both from a theoretical and a numerical point of view. A three-dimensional coordinate system has been built in order to handle the two-directional curved periodicity. This system has been defined from the two helical directions of periodicity and the radial coordinate of the problem. The existence of Bloch waves in bi-helical structures can be justified, somehow *a posteriori*, owing to the independence of the metric tensor of the curvilinear system on both helical coordinates. Because elastodynamic problems correspond to a vector wave equation, Bloch theorem has to be expressed in appropriate bases to project the vector wavefields. It has been shown that these bases can be the

covariant/contravariant bases of the bi-helical system, or alternatively, the cylindrical basis. The three-dimensional geometry of the unit cell, delimited by helicoids, has been carefully built. The problem has been solved numerically thanks to a WFEM approach. The relationship between the two-dimensional propagation constants, which are not independent of each other due to the cylindrical nature of the geometry, has been derived. The wave mode properties (wavenumbers, group and energy velocities) have been calculated along the helical propagation directions as well as the straight and circumferential directions of the problem. The overall approach has been successfully validated by considering uniform tubes and a chiral nanotube taken from the literature. Finally, the method has been applied to a complex multi-wire structure corresponding to the double armor of an energy cable, showing that wave modes propagating predominantly in the individual wires tend to behave freely in the structure as the frequency increases.

Acknowledgements

This work was carried out within the framework of the WEAMEC, West Atlantic Marine Energy Community, and with funding from the Pays de la Loire Region.

References

[1] R. Nelson, S. Dong, R. Kalra, Vibrations and waves in laminated orthotropic circular cylinders, J. Sound Vib. 18 (1971) 429–444.

[2] E. Kausel, An explicit solution for the Green functions for dynamic loads in layered media, MIT Research Report R81-13, Department of Civil Engineering, School of Engineering, Massachusetts Institute of Technology, 1981.

[3] G. Liu, J. Achenbach, Strip element method to analyze wave scattering by cracks in anisotropic laminated plates, J. Appl. Mech. 62 (1995) 607–607.

[4] T. Hayashi, W.-J. Song, J. L. Rose, Guided wave dispersion curves for a bar with an arbitrary cross-section, a rod and rail example, Ultrasonics 41 (2003) 175–183.

[5] I. Bartoli, A. Marzani, F. Lanza di Scalea, E. Viola, Modeling wave propagation in damped waveguides of arbitrary cross-section, Journal of Sound and Vibration 295 (2006) 685–707.

[6] H. Gravenkamp, H. Man, C. Song, J. Prager, The computation of dispersion relations for three-dimensional elastic waveguides using the scaled boundary finite element method, J. Sound Vib. 332 (2013) 3756–3771.

[7] H. Bai, J. Zhu, A. H. Shah, N. Popplewell, Three-dimensional steady state green function for a layered isotropic plate, Journal of Sound and Vibration 269 (2004) 251–271.

[8] F. Treyssède, Three-dimensional modeling of elastic guided waves excited by arbitrary sources in viscoelastic multilayered plates, Wave Motion 52 (2015) 33–53.

[9] D. M. Mead, Wave propagation in continuous periodic structures: Research contributions from southampton, 1964-1995, Journal of Sound and Vibration 190 (1996) 495–524.

[10] L. Gry, C. Gontier, Dynamic modelling of railway track : A periodic model base on a generalized beam formulation, Journal of Sound and Vibration 199 (1997) 531–558.

[11] B. R. Mace, D. Duhamel, M. J. Brennan, L. Hinke, Finite element prediction of wave motion in structural waveguides, The Journal of the Acoustical Society of America 117 (2005) 2835–2843.

[12] A. Srikantha Phani, J. Woodhouse, N. A. Fleck, Wave propagation in two-dimensional periodic lattices, The Journal of the Acoustical Society of America 119 (2006) 1995–2005.

[13] F. Farzbod, M. J. Leamy, Analysis of bloch's method and the propagation technique in periodic structures, Journal of Vibration and Acoustics 133 (2011) 1–7.

[14] M. Collet, M. Ouisse, M. Ruzzene, M. N. Ichchou, Floquet-bloch decomposition for the computation of dispersion of two-dimensional periodic, damped mechanical systems, International Journal of Solids and Structures 48 (2011) 2837–2848.

[15] C. W. Zhou, J. P. Lainé, M. N. Ichchou, A. M. Zine, Wave finite element method based on reduced model for one-dimensional periodic structures, International Journal of Applied Mechanics 7 (2) (2015) 1550018.

[16] A.-C. Hladky-Hennion, Finite element analysis of the propagation of acoustic waves in waveguides, Journal of Sound and Vibration 194 (1996) 119–136.

[17] A. Demma, P. Cawley, M. Lowe, The effect of bends on the propagation of guided waves in pipes, Journal of Pressure Vessel Technology 127 (2005) 328–335.

[18] S. Finnveden, M. Fraggstedt, Waveguide finite elements for curved structures, Journal of Sound and Vibration 312 (4-5) (2008) 644–671.

[19] O. Onipede, S. B. Dong, Propagating waves and end modes in pretwisted beams, Journal of Sound and Vibration 195 (1996) 313–330.

[20] F. Treyssède, Elastic waves in helical waveguides, Wave Motion 45 (4) (2008) 457–470.

[21] F. Treyssède, L. Laguerre, Investigation of elastic modes propagating in multi-wire helical waveguides, Journal of Sound and Vibration 329 (10) (2010) 1702–1716.

[22] Y. Waki, B. R. Mace, M. J. Brennan, Free and forced vibrations of a tyre using a wave/finite element approach, Journal of Sound and Vibration 323 (2009) 737–756.

[23] N. G. Stephen, Y. Zhang, Eigenanalysis and continuum modelling of pre-twisted repetitive beam-like structures, International Journal of Solids and Structures 43 (2006) 3832–3855.

[24] F. Treyssède, Numerical investigation of elastic modes of propagation in helical waveguides, Journal of the Acoustical Society of America 121 (2007) 3398–3408.

[25] F. Maurin, Bloch theorem with revised boundary conditions applied to glide and screw symmetric, quasi-one-dimensional structures, Wave Motion 61 (2016) 20–39.
[26] E. Manconi, B. R. Mace, Wave characterization of cylindrical and curved panels using a finite element method, The Journal of the Acoustical Society of America 125 (1) (2009) 154.
[27] J. M. Renno, B. R. Mace, Calculating the forced response of cylinders and cylindrical shells using the wave and finite element method, Journal of Sound and Vibration 333 (2014) 5340–5355.
[28] A. Nateghi, L. Van Belle, C. Claeys, E. Deckers, B. Pluymers, W. Desmet, Wave propagation in locally resonant cylindrically curved metamaterial panels, International Journal of Mechanical Sciences 127 (2017) 73–90.
[29] E. Manconi, S. Sorokin, R. Garziera, A. Soe-Knudsen, Wave motion and stop-bands in pipes with helical characteristics using wave finite element analysis, Journal of Applied and Computational Mechanics 4 (2018) 420–428.
[30] F. Maurin, C. Claeys, L. Van Belle, W. Desmet, Bloch theorem with revised boundary conditions applied to glide, screw and rotational symmetric structures, Computer Methods in Applied Mechanics and Engineering 318 (2017) 497–513.
[31] F. Treyssède, Free and forced response of three-dimensional waveguides with rotationally symmetric cross-sections, Wave Motiondoi:https://doi.org/10.1016/j.wavemoti.2018.08.001.
[32] T. Chang, J. Geng, X. Guo, Chirality- and size-dependent elastic properties of single-walled carbon nanotubes, Applied Physics Letters 87 (2005) 251929.
[33] M. Buragohain, R. Velmurugan, Study of filament wound grid-stiffened composite cylindrical structures, Composite Structures 93 (2011) 1031–1038.
[34] M. Hemmatnezhad, G. H. Rahimi, R. Ansari, On the free vibrations of grid-stiffened composite cylindrical shells, Acta Mechanica 225 (2) (2014) 609–623.
[35] A. Lopatin, E. Morozov, A. Shatov, An analytical expression for fundamental frequency of the composite lattice cylindrical shell with clamped edges, Composite Structures 141 (2016) 232 – 239.
[36] B. Gustavsen, A. Bruaset, J. J. Bremnes, A. Hassel, A finite-element approach for calculating electrical parameters of umbilical cables, IEEE Transactions on Power Delivery 24 (2009) 2375 – 2384.
[37] W. C. Guttner, C. C. P. Santos, C. P. Pesce, A finite element method assessment of a steel tube umbilical (stu) cable subjected to crushing load: Comparison between two and three-dimensional approaches, Marine Structures 53 (2017) 52–67.
[38] S. Reich, C. Thomsen, J. Maultzsch, Carbon Nanotubes: Basic Concepts and Physical Properties, Wiley-VCH, 2004.
[39] J.-L. Synge, A. Schild, Tensor Calculus, Dover, 1978.
[40] D. Chapelle, K. J. Bathe, The Finite Element Analysis of Shells – Fundamentals, Springer, 2003.
[41] A. Gray, E. Abbena, S. Salamon, Modern Differential Geometry of Curves and Surfaces with Mathematica, 3rd Edition, Chapman & Hall, Boca Raton, 2006.
[42] F. Bloch, Über die quantenmechanik der elektronen in kristallgittern, Zeitschrift für physik 52 (7-8) (1929) 555–600.
[43] T. Garavaglia, J. Gomatam, The schrodinger equation in helical coordinates, Annals of Physics 89 (1975) 1–10.
[44] F. Treyssède, Elastic waves in helical waveguides, Wave Motion 45 (2008) 457–470.
[45] F. Treyssède, M. Ben Tahar, Jump conditions for unsteady small perturbations at fluid-solid interfaces in the presence of initial flow and prestress, Wave Motion 46 (2009) 155–167.
[46] R. S. Langley, A note on the force boundary conditions for two-dimensional periodic structures with corner freedoms 167 (2) (1993) 377–381.
[47] B. R. Mace, E. Manconi, Modelling wave propagation in two-dimensional structures using finite element analysis, Journal of Sound and Vibration 318 (2008) 884–902.
[48] R. Lehoucq, D. Sorensen, C. Yang, ARPACK User's Guide: Solution of Large Scale Eigenvalue Problems with Implicitly Restarted Arnoldi Methods, SIAM, Philadelphia, PA, 1998.
[49] C. Geuzaine, J.-F. Remacle, Gmsh: A 3D finite element mesh generator with builtin pre and postprocessing facilities, International Journal for Numerical Methods in Engineering 79 (11) (2009) 1309–1331.
[50] A. W. Leissa, Vibration of shells, Tech. rep., NASA-SP-288 (1973).
[51] N. C. Perkins, C. D. Mote, Comments on curve veering in eigenvalue problems, Journal of Sound and Vibration 106 (1986) 451–463.
[52] C. Pierre, Mode localization and eigenvalue loci veering in disordered structures, Journal of Sound and Vibration 126 (1988) 485–502.
[53] F. Treyssède, Dispersion curve veering of longitudinal guided waves propagating inside prestressed seven-wire strands, Journal of Sound and Vibration 367 (2016) 56–68.
[54] R. S. Langley, On the modal density and energy flow characteristics of periodic structures, Journal of Sound and Vibration 172 (1994) 491–511.
[55] V. Gerasik, M. Stastna, Complex group velocity and energy transport in absorbing media, Physical Review E - Statistical, Nonlinear, and Soft Matter Physics 81 (2010) 056602.
[56] J. M. Carcione, D. Gei, S. Treitel, The velocity of energy through a dissipative medium, Geophysics 75 (2010) 37–47.

Appendix A. Group and energy velocities in the helical directions

One considers no damping and real values of k_1 and k_2. Taking the differential of Eq. (34) yields:

$$\mathrm{d}\mathbf{A}^*(\mathbf{K}-\omega^2\mathbf{M})\mathbf{A}\tilde{\mathbf{U}} + -2\omega\mathrm{d}\omega\mathbf{A}^*\mathbf{M}\mathbf{A}\tilde{\mathbf{U}} + \mathbf{A}^*(\mathbf{K}-\omega^2\mathbf{M})\mathrm{d}\mathbf{A}\tilde{\mathbf{U}} + \mathbf{A}^*(\mathbf{K}-\omega^2\mathbf{M})\mathbf{A}\mathrm{d}\tilde{\mathbf{U}} = \mathbf{0} \tag{A.1}$$

This equation is used to investigate the effect on frequency of a small change in wavenumbers $\mathrm{d}k_1$ and $\mathrm{d}k_2$. After left-multiplying the above equation by $\tilde{\mathbf{U}}^*$, the last term vanishes due to the fact that $\mathbf{K}$ and $\mathbf{M}$ are hermitian, so that:

$$\tilde{\mathbf{U}}^*\mathrm{d}\mathbf{A}^*(\mathbf{K}-\omega^2\mathbf{M})\mathbf{A}\tilde{\mathbf{U}} - 2\omega\mathrm{d}\omega\tilde{\mathbf{U}}^*\mathbf{A}^*\mathbf{M}\mathbf{A}\tilde{\mathbf{U}} + \tilde{\mathbf{U}}^*\mathbf{A}^*(\mathbf{K}-\omega^2\mathbf{M})\mathrm{d}\mathbf{A}\tilde{\mathbf{U}} = \mathbf{0} \tag{A.2}$$

which can be simplified to:

$$\tilde{\mathbf{U}}^*\mathrm{d}\mathbf{A}^*\mathbf{F} - 2\omega\mathrm{d}\omega\mathbf{U}^*\mathbf{M}\mathbf{U} + \mathbf{F}^*\mathrm{d}\mathbf{A}\tilde{\mathbf{U}} = \mathbf{0} \tag{A.3}$$

Since $\tilde{\mathbf{U}}^*\mathrm{d}\mathbf{A}^*\mathbf{F} = (\mathbf{F}^*\mathrm{d}\mathbf{A}\tilde{\mathbf{U}})^*$, this equation becomes:

$$2\mathrm{Re}(\mathbf{F}^*\mathrm{d}\mathbf{A}\tilde{\mathbf{U}}) = 2\omega\mathrm{d}\omega\mathbf{U}^*\mathbf{M}\mathbf{U} \tag{A.4}$$

From Eq. (33) and the equality $\mathrm{d}\lambda_1 = \mathrm{i}\lambda_1\Delta l_1\mathrm{d}k_1$ (and similar expression for $\mathrm{d}\lambda_2$), the differential of $\mathbf{A}$ times $\tilde{\mathbf{U}}$ can be expressed as follows:

$$\mathrm{d}\mathbf{A}\tilde{\mathbf{U}} = \begin{bmatrix} \mathbf{0} \\ \lambda_1\mathbf{J}_{RB}^{-\mathrm{T}}\mathbf{J}_{LB}^{\mathrm{T}}\mathbf{U}_{LB} \\ \mathbf{0} \\ \lambda_1\lambda_2\mathbf{J}_{RT}^{-\mathrm{T}}\mathbf{J}_{LB}^{\mathrm{T}}\mathbf{U}_{LB} \\ \mathbf{0} \\ \lambda_1\mathbf{J}_{R}^{-\mathrm{T}}\mathbf{J}_{L}^{\mathrm{T}}\mathbf{U}_{L} \\ \mathbf{0} \\ \mathbf{0} \\ \mathbf{0} \end{bmatrix} \mathrm{i}\Delta l_1\mathrm{d}k_1 + \begin{bmatrix} \mathbf{0} \\ \mathbf{0} \\ \lambda_2\mathbf{J}_{LT}^{-\mathrm{T}}\mathbf{J}_{LB}^{\mathrm{T}}\mathbf{U}_{LB} \\ \lambda_1\lambda_2\mathbf{J}_{RT}^{-\mathrm{T}}\mathbf{J}_{LB}^{\mathrm{T}}\mathbf{U}_{LB} \\ \mathbf{0} \\ \mathbf{0} \\ \mathbf{0} \\ \lambda_2\mathbf{J}_{T}^{-\mathrm{T}}\mathbf{J}_{B}^{\mathrm{T}}\mathbf{U}_{B} \\ \mathbf{0} \end{bmatrix} \mathrm{i}\Delta l_2\mathrm{d}k_2 = \begin{bmatrix} \mathbf{0} \\ \mathbf{U}_{RB} \\ \mathbf{0} \\ \mathbf{U}_{RT} \\ \mathbf{0} \\ \mathbf{U}_{R} \\ \mathbf{0} \\ \mathbf{0} \\ \mathbf{0} \end{bmatrix} \mathrm{i}\Delta l_1\mathrm{d}k_1 + \begin{bmatrix} \mathbf{0} \\ \mathbf{0} \\ \mathbf{U}_{LT} \\ \mathbf{U}_{RT} \\ \mathbf{0} \\ \mathbf{0} \\ \mathbf{0} \\ \mathbf{U}_{T} \\ \mathbf{0} \end{bmatrix} \mathrm{i}\Delta l_2\mathrm{d}k_2 \tag{A.5}$$

From Eq. (A.5) and Eq. (A.4), the partial derivative of ω with respect to k_α, which defines the group velocity in the s_α-direction, can be identified as:

$$c_{g_\alpha} = \frac{\partial\omega}{\partial k_\alpha} = \frac{P_{n_\alpha}}{\frac{\omega^2}{2\Delta l_\alpha}\mathbf{U}^*\mathbf{M}\mathbf{U}} \tag{A.6}$$

with:

$$P_{n_1} = \frac{1}{2}\mathrm{Re}(\mathrm{i}\omega(\mathbf{F}_{RB}^*\mathbf{U}_{RB} + \mathbf{F}_{RT}^*\mathbf{U}_{RT} + \mathbf{F}_{R}^*\mathbf{U}_{R})), \quad P_{n_2} = \frac{1}{2}\mathrm{Re}(\mathrm{i}\omega(\mathbf{F}_{LT}^*\mathbf{U}_{LT} + \mathbf{F}_{RT}^*\mathbf{U}_{RT} + \mathbf{F}_{T}^*\mathbf{U}_{T})) \tag{A.7}$$

In the above expressions, it can be checked that P_{n_α} represents the time-averaged power flow on the boundary normal to the helical direction s_α. The denominators in Eq. (A.6) is the time-averaged total energy per unit length in the direction s_α. These expressions coincide with the results obtained in Ref. [54] for straight directions of periodicity.

In damped systems, the physical meaning of group velocity may be not obvious. Conversely, the energy velocity remains well defined in conservative or in absorbing media [55, 56]. The energy velocity c_{e_α} in the direction s_α is defined by:

$$c_{e_\alpha} = \frac{P_{n_\alpha}}{E/\Delta l_\alpha} \tag{A.8}$$

where E is the sum of the time-averaged kinetic and potential energy of the cell. In damped systems, no equipartition occurs between kinetic and potential energy. Based on a FE method, the energy E can be readily calculated from the expression:

$$E = \frac{1}{4}\mathrm{Re}(\mathbf{U}^*\mathbf{K}\mathbf{U}) + \frac{|\omega|^2}{4}\mathrm{Re}(\mathbf{U}^*\mathbf{M}\mathbf{U}). \tag{A.9}$$

Appendix B. Dispersion relation for a thin cylindrical shell based on Flügge theory

Based on Flügge theory, the characteristic equation of the dispersion relation is given by the following polynomial of degree 3 [50]:

$$\Omega^6 - K_2\Omega^4 + K_1\Omega^2 - K_0 = 0 \tag{B.1}$$

where $\Omega^2 = \frac{\rho(1-\nu^2)R^2\omega^2}{E}$ is the non-dimensional frequency. The coefficients K_0, K_1 and K_2 are expressed as follows:

$$\begin{cases} K_2 = 1 + \dfrac{1}{2}(3-\nu)(n^2+\kappa^2) + \beta(n^2+\kappa^2)^2 \\ K_1 = \dfrac{1}{2}(1-\nu)[(3+2\nu)\kappa^2 + n^2 + (n^2+\kappa^2)^2 + \dfrac{3-\nu}{1-\nu}\beta(n^2+\kappa^2)^3] \\ K_0 = \dfrac{1}{2}(1-\nu)[(1-\nu^2)\kappa^4 + \beta(n^2+\kappa^2)^4] + \dfrac{\beta}{2}(1-\nu)[2(2-\nu)\kappa^2n^2 + n^4 - 2\nu\kappa^6 - 6\kappa^4n^2 - 2(4-\nu)\kappa^2n^4 - 2n^6] \end{cases} \tag{B.2}$$

with $\beta = \frac{h^2}{12R^2}$ and $\kappa = k_z R$. The parameter n denotes the circumferential order, which lies inside the infinite set of integers ($n \in \mathbb{Z}$) due to the continuous rotational symmetry (the wavefields dependence can be written in terms of the exponential functions $e^{in\theta}$).